Publication Year	2017
Acceptance in OA@INAF	2020-09-21T10:23:44Z
Title	General relativistic models for rotating magnetized neutron stars in conformally flat spacetime
Authors	Pili, A. G.; BUCCIANTINI, NICCOLO'; Del Zanna, L.
DOI	10.1093/mnras/stx1176
Handle	http://hdl.handle.net/20.500.12386/27451
Journal	MONTHLY NOTICES OF THE ROYAL ASTRONOMICAL SOCIETY
Number	470

Monthly Notices
of the
ROYAL ASTRONOMICAL SOCIETY

MNRAS **470,** 2469–2493 (2017)
Advance Access publication 2017 May 12

doi:10.1093/mnras/stx1176

General relativistic models for rotating magnetized neutron stars in conformally flat space–time

A. G. Pili,[1,2,3]★ N. Bucciantini[1,2,3] and L. Del Zanna[1,2,3]

[1]*Dipartimento di Fisica e Astronomia, Università degli Studi di Firenze, Via G. Sansone 1, I-50019 Sesto F. no (Firenze), Italy*
[2]*INAF – Osservatorio Astrofisico di Arcetri, Largo E. Fermi 5, I-50125 Firenze, Italy*
[3]*INFN – Sezione di Firenze, Via G. Sansone 1, I-50019 Sesto F. no (Firenze), Italy*

Accepted 2017 May 9. Received 2017 May 8; in original form 2017 March 30

ABSTRACT

The extraordinary energetic activity of magnetars is usually explained in terms of dissipation of a huge internal magnetic field of the order of $10^{15–16}$ G. How such a strong magnetic field can originate during the formation of a neutron star (NS) is still subject of active research. An important role can be played by fast rotation: if magnetars are born as millisecond rotators dynamo mechanisms may efficiently amplify the magnetic field inherited from the progenitor star during the collapse. In this case, the combination of rapid rotation and strong magnetic field determine the right physical condition not only for the development of a powerful jet-driven explosion, manifesting as a gamma-ray burst, but also for a copious gravitational waves emission. Strong magnetic fields are indeed able to induce substantial quadrupolar deformations in the star. In this paper, we analyse the joint effect of rotation and magnetization on the structure of a polytropic and axisymmetric NS, within the ideal magneto-hydrodynamic regime. We will consider either purely toroidal or purely poloidal magnetic field geometries. Through the sampling of a large parameter space, we generalize previous results in literature, inferring new quantitative relations that allow for a parametrization of the induced deformation, that takes into account also the effects due to the stellar compactness and the current distribution. Finally, in the case of purely poloidal field, we also discuss how different prescription on the surface charge distribution (a gauge freedom) modify the properties of the surrounding electrosphere and its physical implications.

Key words: gravitation – magnetic field – MHD – stars: magnetars – stars: neutron.

1 INTRODUCTION

Although there is a general consensus concerning the main aspects of the formation of a neutron star (NS), we still lack a precise understanding of many key details of the physical processes that lead from the collapse of the core of a massive progenitor, to the typical compact objects that we observe.

The compact remnant left behind a successful supernova (SN) explosion is an hot and neutron rich object, the so-called proto-NS (PNS), whose complex evolution is characterized by large entropy gradients (Pons et al. 1999), instabilities (Urpin 2010), dynamo (Duncan & Thompson 1992) and intense neutrino-driven winds (Pons et al. 1999). It is only after a typical Kelvin–Helmholtz timescale, ∼100 s after core bounce, that the PNS becomes transparent to neutrinos, it rapidly cools, and reaches a state that is dynamically very close to its final equilibrium (Burrows & Lattimer 1986), even if its thermal and magnetic evolution can last much longer (Viganò et al. 2013), and late phase transitions are still possible (Staff, Ouyed & Jaikumar 2006; Drago & Pagliara 2015; Pili et al. 2016).

It is during this brief lapse of time that the magnetic properties of the resulting NS, such as the magnetic field strength, geometry and distribution, will be set. Once the crust begins to form, it will tend to 'freeze' it in position, and only dissipative effects might then affect its evolution (Viganò et al. 2013). The dynamics of the core collapse is so fast that to first order the core evolves as if it was detached from the outer layers of the surrounding star. Hence, it is reasonable to expect that the magnetic properties might be related to the conditions in the core of the progenitor, like its rotational profile (Duncan & Thompson 1992; Spruit 2009) or the presence of a seed field (Woltjer 1960; Ruderman 1972). However, given the complexity of the problem, it is difficult to establish a clear relation among them.

Among all NSs species, the origin of magnetars is a particularly puzzling problem, since they exhibit the strongest magnetic field of all NSs, with a typical strength of the order of $10^{14–15}$ G. Many evolutionary scenarios have been proposed so far (see Spruit 2009; Ferrario, Melatos & Zrake 2015; Popov 2016 for reviews):

★ E-mail: pili@arcetri.astro.it

© 2017 The Authors
Published by Oxford University Press on behalf of the Royal Astronomical Society

Downloaded from https://academic.oup.com/mnras/article-abstract/470/2/2469/3820933 by INAF Trieste (Osservatorio Astronomico di Trieste) user on 14 July 2020

the magnetar magnetic field can be either completely inherited from the progenitor, as the fossil-field scenario suggests (Woltjer 1960; Ruderman 1972), or generated by dynamo mechanisms during the PNS phase as proposed in the original magnetar model (Duncan & Thompson 1992). In the first hypothesis, the magnetic field is the result of magnetic flux freezing in the core collapse of a strongly magnetized ($\sim 10^4$ G) OB star (Ferrario & Wickramasinghe 2006, 2008). Nevertheless, as pointed out by Spruit (2008), the paucity of suitable magnetized progenitors may be inconsistent with the magnetar birth-rate. On the other hand, if the nascent NS rotates at millisecond period, the inherited magnetic field can be further increased by differential rotation (Burrows et al. 2007) and possible dynamo effects (Bonanno, Rezzolla & Urpin 2003; Rheinhardt & Geppert 2005). In principle after core bounce, or alternatively after a merging event, there is a large amount of available free energy that a huge magnetic field, as high as 10^{17} G, could even be reached. Moreover, the combination of millisecond rotation and magnetar magnetic field can easily drive relativistic outflows whose energetic, of the order of $\sim 10^{49-50}$ergs^{-1}, can even power a typical gamma-ray burst (GRB). This makes proto-magnetars possible engine candidates for GRBs (Usov 1992).

Unfortunately, at present, it is still not clear how the evolution of the rotation of the stellar core proceeds before and after the collapse (Ott et al. 2006). If magnetars progenitors are massive main-sequence stars,[1] the magneto-frictional coupling between the core and the outer envelope during red supergiant phase can substantially spin-down the core before collapse (Heger, Woosley & Spruit 2005; Yoon 2015), unless the progenitor star evolves in a close binary system, where mass accretion and/or tidal synchronization can indeed enhance the rotation (Popov & Prokhorov 2006; Popov 2016). After the core bounce, the minimum rotational period attainable by the newly born PNS depends on its physical conditions (such as its temperature and entropy gradient) and its equation of state (EoS). While theoretical works predict a minimum rotational period $P \sim$ 1–3 ms (Goussard, Haensel & Zdunik 1998; Villain et al. 2004; Camelio et al. 2016), some GRBs light curves, if interpreted within the proto-magnetar model (Bucciantini et al. 2009; Metzger et al. 2011; Bucciantini et al. 2012), point at the possibility of very fast rotators with $P \gtrsim 0.6$ ms (Rowlinson et al. 2014; Rea et al. 2015), near the mass-shedding limit. Interestingly, recent 3D numerical simulations of core collapse SNe have shown that fast rotation can help the onset of neutrino-driven explosions (Nakamura et al. 2014; Gilkis 2016; Takiwaki, Kotake & Suwa 2016), while magneto-rotational instability can grow magnetar strength magnetic fields with a strong toroidal component (Mösta et al. 2015). Efficient magnetic field amplification has been obtained also in NS merging numerical simulations by Giacomazzo et al. (2015) and Kiuchi et al. (2015).

Such numerical studies follow the evolution of the system for, at most, few tens of milliseconds after the birth of the PNS. At this time, the magnetic field configuration is still away from the final one: the magnetic field continues to evolve until a stabilizing crust is formed. Since, in the case of magnetars, the Alfvénic crossing time ($\sim$0.01–0.1 s) is much smaller than the typical Kelvin–Helmholtz time-scale, the magnetic field can in principle decay against instabilities unless a stable equilibrium is reached before a crust forms (Spruit 2008). However, numerical simulations have shown that the initial field may evolve towards a roughly axisymmetric mixed configuration, dubbed as *twisted torus* (TT), able to persist for many Alfvén times (Braithwaite & Spruit 2006; Braithwaite 2009; Mitchell et al. 2015).

The analysis of the long-term effects induced by the magnetic field on the structure and the properties of the NS requires a different approach, that is based on the modelization of equilibrium configurations of magnetized NSs, taking into account the largest possible set of magnetic field morphologies and current distributions. Several authors have dealt with this problem considering purely poloidal or purely toroidal magnetic field in static and/or rotating NSs (Bocquet et al. 1995; Bonazzola & Gourgoulhon 1996; Cardall, Prakash & Lattimer 2001; Konno 2001; Kiuchi & Yoshida 2008; Frieben & Rezzolla 2012; Pili, Bucciantini & Del Zanna 2014; Bucciantini, Pili & Del Zanna 2015; Franzon, Dexheimer & Schramm 2016) but also mixed field configuration in Newtonian gravity (Yoshida & Eriguchi 2006; Lander & Jones 2009; Mastrano et al. 2011; Fujisawa, Yoshida & Eriguchi 2012; Lasky & Melatos 2013; Fujisawa & Kisaka 2014; Glampedakis, Lander & Andersson 2014; Armaza, Reisenegger & Alejandro Valdivia 2015; Fujisawa & Eriguchi 2015; Mastrano, Suvorov & Melatos 2015) or within the framework of general relativity (GR; Ioka & Sasaki 2004; Ciolfi et al. 2009; Ciolfi, Ferrari & Gualtieri 2010; Pili et al. 2014; Uryū et al. 2014; Pili, Bucciantini & Del Zanna 2015; Bucciantini et al. 2015). A common motivation at the base of these works is the characterization of the stellar quadrupole deformation induced by the magnetic field. Fast rotating newly born magnetars, by virtues of such deformations, are currently considered as possible sources of detectable gravitational waves (GWs), especially if the magnetic field is energetically dominated by its toroidal component (Dall'Osso, Shore & Stella 2009). In this case indeed, the magnetically induced deformation is prolate and dissipative processes can lead to the orthogonalization of the spin and the magnetic axes, in order to minimize the total rotational energy (Cutler 2002). At the same time, this 'spin-flip' mechanism maximizes the efficiency of GW emission so that, in principle, the initial spin-down could be mostly due to GWs rather than magnetic braking. Nevertheless Lasky & Glampedakis (2016) and Moriya & Tauris (2016) have recently searched for GW signatures in the light curve of, respectively, short GRBs and superluminous SNe. They have shown that, if interpreted within the proto-magnetar model, the shape of such light curves indicates that most of the rotational energy losses are compatible with the hypothesis that magnetic braking largely prevails over GWs emission. This either implies small stellar deformations, constraining the toroidal field to be $\lesssim 10^{16}$ G, or an inefficient spin-flip mechanism (Lasky & Glampedakis 2016).

In continuity with Pili et al. (2014, hereafter PBD14), Bucciantini et al. (2015, hereafter BPD15) and Pili et al. (2015) that were limited to static equilibria, in this work we perform a vast and detailed parameter study of rapidly rotating magnetized NSs within the framework of GR. This allows us to establish general trends and expectations regarding how different morphologies of the magnetic field and in particular, its coupling with rotation, affects the structure of the star. The analysis of a large set of equilibria provides us the opportunity to extend previous results presented in literature and to derive new quantitative relations between the induced deformations, the energy content of the system and the structure of the magnetic field. In this work, we will consider only strictly

[1] The association of magnetar CXO J164710.2−455216 with the young cluster Westerlund 1 had suggested that some magnetars may originate from high-mass $\gtrsim 40 M_\odot$ main-sequence stars (Muno et al. 2006). Recently, Clark et al. (2014) have provided a number of arguments in favour of the possible origin of CXO J164710.2−455216 in a massive binary system ($\sim 41 + 35 M_\odot$), identifying the putative pre-SN companion with $M = 9 M_\odot$.

Downloaded from https://academic.oup.com/mnras/article-abstract/470/2/2469/3820933 by INAF Trieste (Osservatorio Astronomico di Trieste) user on 14 July 2020

stationary configurations. Hence, although mixed field configurations, and in particular those dominated by the toroidal magnetic field, are favoured on the basis of stability arguments (Akgün et al. 2013), we will consider only axisymmetric configurations with either purely toroidal or purely poloidal magnetic field. Rotating configurations with mixed field have indeed a non-vanishing Poynting vector that prevents to consider them as strictly stationary equilibria.

The paper is organized as follows. In Section 2, we will introduce the general formalism and the governing equations. In Section 3, we describe the numerical scheme and discuss the new features introduced in XNS (see http://www.arcetri.astro.it/science/ahead/XNS/ for an updated version of the code). Our results are presented in Section 4, while conclusions are drawn in Section 5.

2 FORMALISM

Let us briefly introduce here the general formalism that we have used to describe and compute the space–time structure (the metric), the electromagnetic field, and the matter distribution in our equilibrium models for steady state, magnetized and rotating NSs. In the following, we choose the signature (−, +, +, +) for the space–time metric and, unless otherwise stated, we adopt geometrized units with $c = G = \mathrm{M}_\odot = 1$ and with the factor $\sqrt{4\pi}$ reabsorbed in the definition of the electromagnetic fields.

2.1 Metric

Our approach to the numerical solution of Einstein equations together with the equilibrium conditions for the matter distribution and the electromagnetic field is based on the so-called *3+1 splitting* of the space–time metric and fluid quantities (see e.g. Gourgoulhon 2007, 2010; Alcubierre 2008; Baumgarte & Shapiro 2010; Bucciantini & Del Zanna 2011, to which the reader is referred for a detailed description). In such formalism the generic line element can be written in the ADM form (Arnowitt, Deser & Misner 1962)

$$\mathrm{d}s^2 = -\alpha^2 \mathrm{d}t^2 + \gamma_{ij}(\mathrm{d}x^i + \beta^i \mathrm{d}t)(\mathrm{d}x^j + \beta^j \mathrm{d}t), \tag{1}$$

where α is known as *lapse function*, β^i is a purely spatial vector known as *shift vector*, γ_{ij} is the 3-metric induced on the space-like 3-surface of the foliation, and where we have used adapted coordinates: $x^\mu = [t, x^i]$. The components of any 4-vector projected on the space-like 3-surface are referred as its *Eulerian* components. In the following Greek indexes will be used for four-dimensional quantities, while Latin ones for their respective three-dimensional projections.

In the case of a stationary and axisymmetric equilibrium, the space–time is endowed with a stationary Killing vector ξ^μ and an azimuthal Killing vector χ^μ that locally define a time-like 2-plane Π. Any vector v^μ is said to be *toroidal* if it belongs to this plane, *poloidal* if it is perpendicular (Carter 1970, 1973). For those particular forms of the matter-energy distribution, such that the energy–momentum tensor $T^{\mu\nu}$ satisfies the relations (Kundt & Trümper 1966; Carter 1969)

$$\xi_\mu T^{\mu[\nu}\xi^\kappa \chi^{\lambda]} = 0, \quad \chi_\mu T^{\mu[\nu}\xi^\kappa \chi^{\lambda]} = 0, \tag{2}$$

where square brackets indicate antisymmetrization with respect to enclosed indexes, the metric is *circular* and, adopting spherical-like coordinates $x^\mu = [t, r, \theta, \phi]$ (hence $\xi^\mu = (\partial_t)^\mu$ and $\chi^\mu = (\partial_\phi)^\mu$), the line element simplifies to

$$\mathrm{d}s^2 = -\alpha^2 \mathrm{d}t^2 + \psi^4(\mathrm{d}r^2 + r^2 \mathrm{d}\theta^2) + R^2(\mathrm{d}\phi - \omega \mathrm{d}t)^2. \tag{3}$$

Here, $R = \sqrt{\gamma_{\phi\phi}}$ is knows as *quasi-isotropic radius*, ψ is a *conformal factor* and $\omega = -\beta^\phi$. The determinant of the 3-metric is then $\sqrt{\gamma} = Rr\psi^4$.

The energy–momentum tensor of a fluid at thermodynamic equilibrium equipped with an electromagnetic field, in the absence of magnetization effects (Chatterjee et al. 2015; Franzon et al. 2016), can be written as

$$T^{\mu\nu} = \rho h u^\mu u^\nu + p g^{\mu\nu} + F^\mu_\lambda F^{\nu\lambda} - \frac{1}{4}(F^{\lambda\kappa}F_{\lambda\kappa})g^{\mu\nu}, \tag{4}$$

where ρ is the rest mass density, $h = (e + p)/\rho$ the specific enthalpy, e the energy density, $p = p(\rho, e)$ the pressure (provided by some form of EoS), u^μ is the fluid 4-velocity and $F^{\mu\nu}$ is the Faraday electromagnetic tensor. The electromagnetic tensor can be defined either in terms of the comoving magnetic and electric field b^μ and e^μ (whenever a flow velocity can be defined), or in terms of the so-called *Eulerian* electric and magnetic field E^μ and B^μ (purely spatial vectors), following the same 3+1 splitting of the metric (Del Zanna et al. 2007; Bucciantini & Del Zanna 2011). In the region of space occupied by matter, the ideal MHD condition is $e^\mu = u_\nu F^{\mu\nu} = 0$, and only the comoving magnetic field does not vanish. When this condition is relaxed, non-ideal effects such as dynamo or reconnection processes may take place in both the interior and the magnetosphere of magnetars. For applications to the numerical modelling of relativistic plasmas, see Bucciantini & Del Zanna (2013) and Del Zanna et al. (2016).

Given the ideal-plasma stress energy tensor in equation (4), under the assumption of stationarity and axisymmetry, the circularity condition holds provided the 4-velocity is toroidal, i.e. $u^r = u^\theta = 0$, and the magnetic field is either purely toroidal or purely poloidal. However it can be shown (Oron 2002), and it has been verified (Shibata & Sekiguchi 2005; Dimmelmeier, Stergioulas & Font 2006; Ott et al. 2007; Bucciantini & Del Zanna 2011, PBD14) that, considering purely toroidal flow, the metric can be safety simplified neglecting off-diagonal terms (with the exception of β^ϕ), even for a mixed magnetic field. In particular, even for highly deformed star up to the *mass shedding limit* and/or for magnetic field with strength up to 10^{19}G, the difference between R and $\psi^2 r \sin\theta$ is at most of the order of 10^{-3}, so one can assume to a high level of accuracy that the metric is *conformally flat* (CFC assumption; Isenberg 2008; Wilson & Mathews 2003):

$$\mathrm{d}s^2 = -\alpha^2 \mathrm{d}t^2 + \psi^4[\mathrm{d}r^2 + r^2 \mathrm{d}\theta^2 + r^2 \sin^2\theta(\mathrm{d}\phi - \omega \mathrm{d}t)^2], \tag{5}$$

with the volume element of the 3-metric given by $\sqrt{\gamma} = \psi^6 r^2 \sin\theta$.

Einstein equations in the CFC approximation can be conveniently recast into a set of elliptical partial differential equations (PDEs) for the metric quantities α, ψ and ω, where the source terms contain the information about the energy–momentum distribution (Dimmelmeier, Font & Müller 2002; Bucciantini & Del Zanna 2011):

$$\Delta\psi = -\left[2\pi E + \frac{1}{8}K_{ij}K^{ij}\right]\psi^5, \tag{6}$$

$$\Delta(\alpha\psi) = \left[2\pi(E + 2S) + \frac{7}{8}K_{ij}K^{ij}\right]\alpha\psi^5, \tag{7}$$

$$\Delta\omega = -16\pi\alpha\psi^4 S^\phi - 2\psi^{10}K^{\phi j}\nabla_j(\alpha\psi^{-6}). \tag{8}$$

Here, Δ and ∇ are the standard *Laplacian* and *Gradient* operator with respect to the 3-metric γ_{ij}, K^{ij} is the extrinsic curvature and the source term are given by

$$E = \rho h \Gamma^2 - p + \frac{1}{2}(E^i E_i + B^i B_i), \tag{9}$$

Downloaded from https://academic.oup.com/mnras/article-abstract/470/2/2469/3820933 by INAF Trieste (Osservatorio Astronomico di Trieste) user on 14 July 2020

$$S = \rho h(\Gamma^2 - 1) + 3p + \frac{1}{2}(E^i E_i + B^i B_i), \tag{10}$$

$$S_\phi = \rho h \Gamma v_\phi + \epsilon_{\phi jk} E^j B^k, \tag{11}$$

where ϵ_{ijk} is the three-dimensional Levi-Civita alternating tensor and the ϕ-component of the 3-velocity v^ϕ is linked to u^ϕ through the Lorentz factor Γ by $u^\phi = \Gamma(v^\phi - \beta^\phi/\alpha)$, where the normalization $u^\mu u_\mu = -1$ implies $\Gamma = (1 - v^2)^{-1/2}$.

2.2 Electromagnetic fields

The 3+1 splitting allows one to write the Maxwell equations:

$$\nabla_\mu F^{\mu\nu} = -j^\nu, \quad \nabla_\mu(\epsilon^{\mu\nu\lambda\kappa} F_{\lambda\kappa}) = 0, \tag{12}$$

where j^μ is the *4-current density*, and $\epsilon^{\mu\nu\lambda\kappa}$ four-dimensional Levi-Civita alternating tensor, in terms of the Eulerian electric and magnetic field $E^i = [E^r, E^\theta, E^\phi]$, $B^i = [B^r, B^\theta, B^\phi]$. The stationary Maxwell equations in the $3 + 1$ formalism can be written in a compact form using standard three-dimensional vector quantities, and the related divergence and curl operators defined with respect to the diagonal 3-metric γ_{ij}:

$$\boldsymbol{\nabla} \cdot \boldsymbol{B} = 0, \tag{13}$$

$$\boldsymbol{\nabla} \times (\alpha \boldsymbol{E} + \boldsymbol{\beta} \times \boldsymbol{B}) = 0, \tag{14}$$

$$\boldsymbol{\nabla} \cdot \boldsymbol{E} = \rho_e, \tag{15}$$

$$\boldsymbol{\nabla} \times (\alpha \boldsymbol{B} - \boldsymbol{\beta} \times \boldsymbol{E}) = \alpha \boldsymbol{J} - \rho_e \boldsymbol{\beta}, \tag{16}$$

where ρ_e is the charge density, and corresponds to the time-like component of the 4-current j^μ, while $\boldsymbol{J}$ is its three-dimensional space-like projection.

Equation (13) implies that the magnetic field can be written as the curl of vector potential $\mathbf{A}$ such that $B^i = \varepsilon^{ijk}\partial_j(A_k)$. This, together with the assumption of axisymmetry, $\partial_\phi = 0$, implies that the poloidal (r, θ) components of the magnetic field can be expressed in terms of the gradient of a scalar function $\Psi(r, \theta) \equiv A_\phi$, called *magnetic flux function*. Analogously the ϕ-component of the magnetic field can be written using another scalar function $\mathcal{I}$ ($B_\phi = \alpha^{-1}\mathcal{I}$) known as *current function*. By introducing the orthonormal triad the magnetic vector field can be expressed as

$$\boldsymbol{B} = \frac{\boldsymbol{\nabla}\Psi}{R} \times \boldsymbol{e}_{\hat{\phi}} + \frac{\mathcal{I}}{\alpha R}\boldsymbol{e}_{\hat{\phi}}, \tag{17}$$

where $\nabla\Psi$ is the vector field associated with the gradient of Ψ with components $(\nabla\Psi)_{\hat{i}} = \partial_i\Psi/\sqrt{\gamma_{ii}}$. The isosurfaces $\Psi(r, \theta) = cost$, are known as *magnetic surfaces*, and any scalar function f satisfying $\boldsymbol{B} \cdot \boldsymbol{\nabla} f = 0$ will be constant on them: $f = f(\Psi)$.

It is possible to show, starting from equation (16), that the poloidal component of the 3-current is related to the curl of the azimuthal magnetic field, $\alpha J^i = \varepsilon^{ij\phi}\partial_j(\alpha B_\phi)$, such that

$$\boldsymbol{J} = \frac{\boldsymbol{\nabla}\mathcal{I}}{\alpha R} \times \boldsymbol{e}_{\hat{\phi}} + J_{\hat{\phi}}\boldsymbol{e}_{\hat{\phi}}, \tag{18}$$

where

$$\frac{\alpha}{R} J_{\hat{\phi}} = -\nabla \cdot \left(\frac{\alpha}{R^2}\nabla\Psi\right) + \boldsymbol{E} \cdot \nabla\omega. \tag{19}$$

From the other sourceless Maxwell equation, equation (14), under the same constraints of stationarity and axisymmetry, one finds $\alpha E_\phi = 0$. The same equation implies that the poloidal components can be written as the gradient of a scalar function Φ as

$$\alpha \boldsymbol{E} + \boldsymbol{\beta} \times \boldsymbol{B} = \alpha \boldsymbol{E} - \omega\boldsymbol{\nabla}\Psi = \boldsymbol{\nabla}\Phi. \tag{20}$$

Assuming conformal flatness, equation (5), the Maxwell–Gauss equation, equation (15), can be written as an elliptical PDE for the electromagnetic potentials Φ and Ψ, as a function of the charge and current density.

$$\begin{aligned}\Delta\Phi = {} & \psi^4\left[\alpha\rho_e + \omega\psi^4 r^2 \sin^2\theta J^\phi\right] - \frac{\omega\psi^4 r^2 \sin^2\theta}{\alpha^2}\partial\omega\partial\Phi \\ & \times \left[1 + \frac{\omega^2\psi^4 r^2 \sin^2\theta}{\alpha^2}\right]\partial\omega\partial\Psi - \partial\ln(\alpha^{-1}\psi^2) \\ & \times [\partial\Phi + 2\omega\partial\Psi] - \frac{2\omega}{r}\left[\partial_r\Psi + \frac{1}{r\tan\theta}\partial_\theta\Psi\right].\end{aligned} \tag{21}$$

The same can be done for the Maxwell–Ampère equation (16):

$$\begin{aligned}\tilde{\Delta}_3\tilde{\Psi} = {} & \psi^4 r\sin\theta\left(\frac{\partial\omega\partial\Phi + \omega\partial\omega\partial\Psi}{\alpha^2} - \psi^4 J^\phi\right) \\ & + \partial\ln(\alpha^{-1}\psi^2)\partial\Psi,\end{aligned} \tag{22}$$

where, for convenience, we have introduced the quantity $\tilde{\Psi} = \Psi/(r\sin\theta)$, and the new operators are defined as in PBD14:

$$\partial f\partial g = \partial_r f\partial_r g + \frac{1}{r^2}\partial_\theta f\partial_\theta g, \tag{23}$$

$$\tilde{\Delta}_3 = \Delta - \frac{1}{r^2\sin^2\theta}. \tag{24}$$

These equations completely define the electromagnetic field in the entire space, once the charge and current distribution are known, independently of the fluid properties.

If there is an observer that measures a vanishing electric field in his reference frame (for example if one assumes the NS to be perfectly conducting, the comoving electric field inside vanishes), then the condition $\boldsymbol{E} \cdot \boldsymbol{B} = 0$ holds. This establishes a relation between the two electromagnetic potentials: $\boldsymbol{B} \cdot \nabla\Phi = 0 \Rightarrow \Phi = \Phi(\Psi)$. In such a situation one can introduce a velocity $\boldsymbol{v}$ so that

$$\boldsymbol{E} = -\boldsymbol{v} \times \boldsymbol{B}, \tag{25}$$

where, defining $\Omega = \Omega(\Psi) = -\mathrm{d}\Phi/\mathrm{d}\Psi$, we have

$$\boldsymbol{v} = v\,\boldsymbol{e}_{\hat{\phi}} \quad \text{with} \quad v = \frac{R(\Omega - \omega)}{\alpha}\boldsymbol{e}_{\hat{\phi}}. \tag{26}$$

Notice that here Ω represents the rotational rate of the magnetic field lines with respect to infinity. Is then possible to express the electric field and the charge density in terms of the magnetic flux function:

$$\boldsymbol{E} = -\frac{\Omega - \omega}{\alpha}\boldsymbol{\nabla}\Psi, \tag{27}$$

$$\rho_e = -\boldsymbol{\nabla} \cdot \left(\frac{\Omega - \omega}{\alpha}\boldsymbol{\nabla}\Psi\right). \tag{28}$$

As long as the magnetic field is confined inside the NS, so is also the electric field. However this condition can naturally be enforced only for toroidal magnetic field, where the electric field vanishes by construction. In the case of a poloidal magnetic field this is expected to extend outside the NS surface (Ciolfi et al. 2009, 2010; Lander & Jones 2009; Ciolfi & Rezzolla 2013; PBD14, BPD15), unless an ad hoc singular toroidal current is added at the surface itself (Fujisawa & Eriguchi 2015). One then needs to define the condition holding outside the NS surface, in order to decide how to extend the field from the interior, where

Downloaded from https://academic.oup.com/mnras/article-abstract/470/2/2469/3820933 by INAF Trieste (Osservatorio Astronomico di Trieste) user on 14 July 2020

the typically high conductivity of degenerate matter can enforce ideal MHD.

2.2.1 *Outer vacuum*

The general assumption that is made in the literature (Bocquet et al. 1995; Franzon et al. 2016), and the one that for consistency is adopted in this work, is that outside the NS is surrounded by a vacuum. In this case one cannot define any meaningful reference frame in the exterior, such that it is not possible to enforce any relation between Ψ and Φ. The equations of the potentials must be solved separately assuming $\rho_e = J^\phi = 0$, only subject to the requirement of continuity at the stellar surface. In this case it is well known (Goldreich & Julian 1969; Michel & Li 1999) that one will have regions with $\boldsymbol{E}\cdot\boldsymbol{B} \neq 0$, which are known as *vacuum gaps*. Moreover, as we will discuss in Section 3.1 the solution is not unique.

2.2.2 *Force-free limits*

On the other hand if one assume the existence of a low-density plasma, that, without affecting the dynamics can provide the required changes and currents, the condition $\boldsymbol{E}\cdot\boldsymbol{B} = 0$ can be extended outside the NS surface. This is the base of the so-called *degenerate electro-dynamics*, and it is the prescription generally adopted in magnetospheric models that focus just on the exterior (Michel 1973; Contopoulos, Kazanas & Fendt 1999; Spitkovsky 2006; Timokhin 2006; Tchekhovskoy, Spitkovsky & Li 2013; Pétri 2016), and that has been recently extended to global models (Ruiz, Paschalidis & Shapiro 2014). In this case, the Lorentz force per unit volume acting on the plasma is

$$\boldsymbol{L} = \rho_e\boldsymbol{E} + \boldsymbol{J}\times\boldsymbol{B} = (\boldsymbol{J} - \rho_e\boldsymbol{v})\times\boldsymbol{B}, \tag{29}$$

which, using equations (17) and (18), becomes

$$\boldsymbol{L} = \left(\frac{J_{\hat\phi}}{R} - \rho_e\frac{v}{R}\right)\nabla\Psi - \frac{\mathcal{I}\,\nabla\mathcal{I}}{\alpha^2R^2} + \frac{\nabla\mathcal{I}\times\nabla\Psi\cdot\boldsymbol{e}_{\hat\phi}}{\alpha R^2}\,\boldsymbol{e}_{\hat\phi}. \tag{30}$$

Given the negligible dynamical effects of the plasma the Lorentz force must vanish: $\boldsymbol{L} = 0$. This case is referred as force-free electrodynamics (FFE). One may notice immediately that the azimuthal component of the Lorentz force vanishes if, and only if, $\mathcal{I} = \mathcal{I}(\Psi)$. Hence,

$$\boldsymbol{L} = \left(\frac{J_{\hat\phi}}{R} - \frac{\mathcal{I}}{\alpha^2R^2}\frac{\mathrm{d}\mathcal{I}}{\mathrm{d}\Psi} - \rho_e\frac{\Omega-\omega}{\alpha}\right)\nabla\Psi = 0. \tag{31}$$

By making use of equation (19), this can be written as a single equation for Ψ, known as the relativistic *Grad–Shafranov equation*. After some algebra one recovers the *pulsar equation*:

$$\nabla\cdot\left[\frac{\alpha}{R^2}\left(1-v^2\right)\nabla\Psi\right] + \frac{v}{R}\frac{\mathrm{d}\Omega}{\mathrm{d}\Psi}|\nabla\Psi|^2 + \frac{\mathcal{I}}{\alpha R^2}\frac{\mathrm{d}\mathcal{I}}{\mathrm{d}\Psi} = 0. \tag{32}$$

Notice that in the force-free regime there is nothing to prevent $v > 1$, being this just the drift velocity associated with the motion of immaterial field lines. This happens at a surface defined by $R = R_{\rm L} = \alpha(\Omega-\omega)^{-1}$ and called *Light Cylinder*. Regularity of the solution of the Grad–Shafranov equation at such surface introduces further constraints on $\mathcal{I}(\Psi)$. Note that contrary to solutions in vacuum, where there is no net energy flow associated with the outer electromagnetic field, in the FFE case there is a net energy flow along those field lines that cross the Light Cylinder. This implies that the FFE assumption is not fully consistent with our requirement of a strict stationary system.

2.3 Matter

Let us discuss here the equilibrium conditions for the matter distribution, under the simultaneous action of gravity and an electromagnetic field. Here, we will consider for simplicity a toroidal flow

$$u^\mu = u^t(1,0,0,\Omega), \quad \Omega \equiv u^\phi/u^t, \tag{33}$$

where now Ω is the fluid angular velocity as measured by an observer at rest at spatial infinity. Notice that within the ideal MHD regime, the angular velocity appearing in the Ohm's law [that is the same as in (25)] actually coincides with the fluid rotational rate.

The requirement of stationarity implies that the rotational rate Ω should be constant on magnetic surfaces. However, very ad hoc forms for the angular momentum distribution and the current distribution are required in order to satisfy such requirement. For example the simplest prescription of *constant specific angular momentum* leads to a rotation largely stratified on cylinders, known as *von Zeipel cylinders* (von Zeipel 1924), while the simplest prescriptions for the current distribution (Ciolfi et al. 2009; Lander & Jones 2009; PBD14) lead to dipole-like magnetic surfaces. The other possibility is to consider solid body rotation with $\Omega = \text{const}$ (Oron 2002), as we do in this work. In this case the ideal MHD condition $\nabla\Phi = -\Omega\nabla\Psi$ can be easily integrated in

$$\Phi = -\Omega\Psi + C, \tag{34}$$

where C is an integration constant that define the arbitrary monopolar charge of the star.

The dynamics of matter is described by the relativistic *Euler equation*, which in the presence of a generic external force (per unit volume) f_μ is

$$\rho h a_\mu + \partial_\mu p + u_\mu u^\nu\partial_\nu p = f_\mu, \tag{35}$$

where a^μ is the 4-acceleration. Recalling that $u^i = 0, (i = r,\theta)$ and $\partial_t = \partial_\phi = 0$, so that $u^\nu\partial_\nu = 0$, one has

$$a_\mu = u^\nu\left(\partial_\nu u_\mu - \Gamma^\lambda_{\mu\nu}u_\lambda\right) = -\frac{1}{2}u^\nu u^\lambda\partial_\mu g_{\nu\lambda}, \tag{36}$$

and its spatial projection in the $3+1$ formulation is

$$a_i = \frac{\Gamma^2}{2\alpha^2}\left[\partial_i(\alpha^2 - R^2\omega^2) + 2\Omega\partial_i(R^2\omega) - \Omega^2\partial_i R^2\right]. \tag{37}$$

Recalling the definition of v, and given the relation $v^2\Gamma^2\partial_i\ln v = \partial_i\ln\Gamma$, one finally gets

$$\frac{\partial_i p}{\rho h} + \partial_i\ln\alpha - \partial_i\ln\Gamma = \frac{L_i}{\rho h}, \tag{38}$$

where we have also specialized the external force to the Lorentz force L_i. Notice that axisymmetry implies necessarily $f_\phi = 0$, whatever the nature of the force.

In order to cast this equation into an integrable form, suitable for numerical solutions, two assumptions are required:

(i) a barotropic EoS $p = p(\rho)$, as in the case of a polytropic law:

$$p = K\rho^{1+1/n} \Rightarrow h = 1 + (n+1)K\rho^{1/n}, \tag{39}$$

where n is the *polytropic index*, such that $\partial_i p/(\rho h) = \partial_i\ln h$.

(ii) an external conservative force with potential $\mathcal{M}$:

$$\boldsymbol{L} = \rho h\nabla\mathcal{M}. \tag{40}$$

The first one is usually justified by the fact that matter in NSs can be considered fully degenerate (zero temperature). The second one, on the other hand, restricts the possible choices of the current

Downloaded from https://academic.oup.com/mnras/article-abstract/470/2/2469/3820933 by INAF Trieste (Osservatorio Astronomico di Trieste) user on 14 July 2020

distribution (see e.g. Akgün et al. 2013 for examples where this constrain is relaxed), but is the only one that permits to compute equilibria in the fully non-perturbative regime.

Under those two assumptions one can integrate Euler's equation to derive the so-called *Bernoulli integral*:

$$\ln\frac{h}{h_c}+\ln\frac{\alpha}{\alpha_c}-\ln\frac{\Gamma}{\Gamma_c}=\mathcal{M}-\mathcal{M}_c, \tag{41}$$

where we have indicated with the label c a reference position, for instance the centre of a rotating NS.

Interestingly the MHD condition in equation (34), together with the requirement of integrability, can be easily translated into a condition on the charge and current distribution:

$$\rho_e=\frac{R^2(\Omega-\omega)}{\alpha}\rho h\Gamma^2\frac{\mathrm{d}\mathcal{M}}{\mathrm{d}\Psi}-\frac{\Omega-\omega}{\alpha\psi^4v^2}\partial\ln\Gamma^2\partial\Psi-\frac{1}{\psi^4}\partial\omega\partial\Psi, \tag{42}$$

$$J^\phi=\rho h\Gamma^2\frac{\mathrm{d}\mathcal{M}}{\mathrm{d}\Psi}-\frac{1}{\psi^8r^2\sin^2\theta}\partial\ln\Gamma^2\partial\Psi+\frac{\omega-\Omega}{\alpha^2\psi^4}\partial\omega\partial\Psi. \tag{43}$$

Note, however, that it is not sufficient to impose these forms for the source terms into equation (21) in order to ensure ideal MHD inside the NS because equation (21) defines the electromagnetic field minus an arbitrary harmonic function. This harmonic function (which guarantees ideal MHD inside) corresponds to a singular source term (a surface charge), that have been neglected in deriving the integrability conditions, where we only considered distributed forces.

2.4 Currents

The morphology of the magnetic field is entirely controlled by the analytic form of the free functions $\mathcal{M}$ and $\mathcal{I}$. As discussed in the previous section, the magnetization function $\mathcal{M}$ is associated with the Lorentz force term appearing in the Euler equation, equation (38). The current function $\mathcal{I}$, instead, is strictly related only to the toroidal component of the magnetic field.

If the magnetic field has a poloidal component then $\Psi\neq0$ and $\mathcal{M}$ can be expressed as a function of the magnetic potential Ψ alone because of the orthogonality relation $\boldsymbol{L}\cdot\boldsymbol{B}=0$. A common choice is to express $\mathcal{M}$ as a linear function of Ψ (Ciolfi et al. 2009; Lander & Jones 2009) even if more general analytic forms, including also a non-linear dependence, have been recently investigated (Fujisawa et al. 2012; Ciolfi & Rezzolla 2013; Bera & Bhattacharya 2014, BPD15). In particular, as in BPD15, we adopt

$$\mathcal{M}(\Psi)=k_{\rm pol}\Psi\left(1+\frac{\xi}{|\nu+1|}\Psi^\nu\right), \tag{44}$$

where $k_{\rm pol}$ is the so-called poloidal magnetization constant, ν is the poloidal magnetization index of the non-linear term. Given that the effect of non-liner terms have been already discussed in (BPD15), in this work we will focus on configurations with $\xi=0$, in order to limit the parameter space.

Notice that, in the definition of toroidal currents distribution J^ϕ and of the charge density ρ_e, equations (42) and (43), only the magnetization functions $\mathcal{M}$ enters. This because in purely poloidal configurations $\mathcal{I}=0$. $\mathcal{I}$ in fact encodes information about the poloidal currents distribution, and is different from zero only in the presence of a toroidal magnetic field. However, in the case of a purely toroidal magnetic field, $\Psi=0$ and $\mathcal{M}$ can now be directly connected to $\mathcal{I}$. Indeed, using equation (30) with $\Psi=$ const, the integrability condition in equation (40) reads:

$$\nabla\mathcal{M}=-\frac{\mathcal{I}\nabla\mathcal{I}}{\rho h\alpha^2R^2}. \tag{45}$$

Defining the new quantity $G=\rho h\alpha^2R^2$ the previous equation can be easily integrated if we assume a barotropic-like dependence for the current function $\mathcal{I}=\mathcal{I}(G)$, namely

$$\mathcal{I}=K_{\rm m}G^m, \tag{46}$$

where $K_{\rm m}$ is the *toroidal magnetization constant* and $m\geq1$ is the *toroidal magnetization index* (see also Kiuchi & Yoshida 2008; Lander & Jones 2009, FR12; Fujisawa 2015). With this assumption the magnetization function $\mathcal{M}$ is given by

$$\mathcal{M}=-\frac{mK_{\rm m}^2}{2m-1}G^{2m-1}, \tag{47}$$

and the magnetic field is related to the enthalpy per unit volume through

$$B_\phi=\alpha^{-1}K_{\rm m}G^m=\alpha^{-1}K_{\rm m}(\rho h\,\alpha^2R^2)^m. \tag{48}$$

Here, the magnetization constant $K_{\rm m}$ regulates the strength of the magnetic field (more specifically the magnetic flux trough the meridional plane), while the magnetization index m is related to the distribution of the magnetic field inside the star.

In this work, we will consider exclusively purely poloidal or purely toroidal magnetic fields with all the currents confined inside the star with, at most the addiction of surface terms. In general, rotation with mixed morphologies leads to configurations where the Poynting vector does not vanish and, hence again, the system cannot be considered strictly stationary.

3 NUMERICAL SCHEME

The numerical equilibrium models presented in this work are obtained through the XNS code. This code has been already used to compute equilibrium solutions for static configurations with different topologies of the magnetic field (PBD14, BPD15; Pili et al. 2015), or for rotating unmagnetized star with realistic EoSs (Pili et al. 2016). It has also been extensively validated in the Newtonian-limit (Das & Mukhopadhyay 2015; Mukhopadhyay 2016; Bera & Bhattacharya 2016). In particular, Subramanian & Mukhopadhyay (2015) have verified that XNS provides solutions that are indistinguishable, within the numerical accuracy, from those obtained with other numerical codes. In this work, the XNS code has been modified to handle rotating configurations endowed with a poloidal magnetic field. For the reader convenience, we briefly summarize here its main features (see Bucciantini & Del Zanna 2011 and PBD14 for a complete and detailed description), while in the next subsection we will discuss in more detail our modifications.

The XNS code solves self-consistently the Einstein–Maxwell equations system in the case of an axisymmetric and stationary space–time under the hypothesis of conformal flatness and maximal slicing. The metric solver operates in the so-called eXtended Conformally Flat Condition (XCFC; Cordero-Carrión et al. 2009), which extends the CFC equations (6)–(8) in a numerical stable form that can be solved using standard and accurate numerical techniques, with a typical relative error 10^{-4} with respect to the exact GR solution (Bucciantini & Del Zanna 2011, PBD14). The main idea at the base of XCFC is to express K^{ij} in terms of an auxiliary vector W^i which is related to the longitudinal part of K^{ij} itself. The transverse-traceless component of the extrinsic curvature K^{ij} is

Downloaded from https://academic.oup.com/mnras/article-abstract/470/2/2469/3820933 by INAF Trieste (Osservatorio Astronomico di Trieste) user on 14 July 2020

instead neglected, being typically smaller that the non-conformal content of the spatial metric.

Einstein equations are turned into a system of two scalar Poisson-like Partial Differential Equations (PDEs), one for the conformal factor ψ and one for the lapse function α, and two vector Poisson-like equations, one for the shift vector β^i and the other for W^i. Such equations are fully decoupled so that they can be solved hierarchically (first the one for W^i, then ψ, α and finally β^i). Moreover, they can be cast into a form that guarantees the *local uniqueness*.

In the case of rotating stars with no meridional flow (i.e. $v^r = v^\theta = 0$) only W^ϕ and β^ϕ are different from zero. The PDEs associated with these two quantities have the general form:

$$\Delta X^{\hat{\phi}} = H^{\hat{\phi}}, \tag{49}$$

where the $\boldsymbol{X} = \boldsymbol{X}(r, \theta)$ is the generic unknown vector field and $\boldsymbol{H}$ is the associated source term. For W^ϕ, the source term depends on S^ϕ. For $\omega = -\beta^\phi$ (solved at the end), $\boldsymbol{H}$ depends also on previously determined quantities. Analogously the PDEs for α and ψ can be generally written as

$$\Delta q = s q^p, \tag{50}$$

where, again, $q = q(r, \theta)$ is the generic unknown function while s is the scalar source term which depends on the stress-energy content of the space–time and on previously computed metric terms.

Solutions to these equations are computed with a semispectral method. The scalar functions, such as ψ, α and Φ, are expanded into a linear combination of spherical harmonics $Y_\ell(\theta)$

$$q(r, \theta) = \sum_{\ell=0}^{\infty} C_\ell(r) Y_\ell(\theta), \tag{51}$$

while vector quantities W^ϕ, β^ϕ and Ψ are expanded as

$$X^\phi(r, \theta) = \sum_{\ell=0}^{\infty} K_\ell(r) Y'_\ell(\theta), \tag{52}$$

where $'$ stands for the derivative with respect to θ (notice that axisymmetry excludes the harmonic degrees $m \neq 0$). Adopting a second order radial discretization, the harmonic expansion reduces each PDE to a set of radial ordinary differential equations, one for each coefficient $C_\ell(r)$ (or analogously K_ℓ), that is solved via direct inversion of tridiagonal matrices. The harmonic decomposition ensures also the correct behaviour of the solution on the symmetry axis, at the centre and at the outer boundary of the domain which, in our case, is set at a finite distance from the stellar surface. In particular, at the centre of the star the harmonic coefficients C_ℓ and K_ℓ go to zero with parity $(-1)^\ell$ and $(-1)^{\ell+1}$, respectively, while at the outer radius they scale as $r^{-(\ell+1)}$.

Remarkably Maxwell equations (21) and (22) share the same mathematical structure of XCFC equations: the scalar equation for Φ is equivalent to equation (50); the equation for Ψ (the ϕ-component of the magnetic potential) is a vector Poisson-like equation analogous to equation (49) where $H = H(\Psi, \partial\Psi)$.

3.1 Numerical resolution of Maxwell equations

In the case of rotating NSs with a purely poloidal field, we solve separately equations (22) and (21), for the potential Ψ and Φ, respectively. Equations are iteratively solved with the source terms given by equations (42) and (43). Accordingly with the vacuum assumption, the current density J^ϕ and the charge density ρ_e are set to zero outside the star.

Since equations (22) and (21) are solved at once on the numerical grid both Ψ and Φ extends smoothly outside the star. This is not consistent with the fact that a magnetized rotating perfect conductor naturally acquires a surface charge density, which in turn manifests in the derivatives of Φ. Indeed, as anticipated in Section 2.3, the newly obtained potential Φ does not satisfy the perfect conducting relation (34) inside the star but differs from the MHD solution $\Phi_{\rm MHD} = -\Omega\Psi + C$ by an harmonic function Φ_a

$$\Phi = \Phi_{\rm MHD} + \Phi_a \quad \text{with} \quad \Delta\Phi_a = 0. \tag{53}$$

This harmonic function Φ_a, can be set by requiring equation (34) to hold just at the stellar surface $\mathcal{S}_{\rm NS}$:

$$\Phi_a|_{\mathcal{S}_{\rm NS}} = (\Phi - \Phi_{\rm MHD})|_{\mathcal{S}_{\rm NS}}. \tag{54}$$

Being an harmonic function, it can be expanded in spherical harmonics as

$$\Phi_a = \sum_{l=0}^{N_\ell} Y_\ell(\theta) \times \begin{cases} a_\ell r^\ell & \text{inside the star,} \\ b_\ell r^{-(\ell+1)} & \text{outside the star.} \end{cases} \tag{55}$$

The coefficients a_ℓ and b_ℓ are found by solving the $N_\ell + 1$ equations that derive from the evaluation of equation (54) on $N_\ell + 1$ collocation points located along the surface $\mathcal{S}_{\rm NS}$. These points are not evenly distributed: in the case of highly oblate NSs, a proper redistribution of the collocation points is chosen in order to improve the convergence and avoid aliasing effects. In particular, while for the interior solution the collocation points are mainly distributed in the vicinity of the stellar equator (at larger radii), in the other case they are clustered near the pole. In addition, points do not coincide with any of the grid-point locating $\mathcal{S}_{\rm NS}$ but they are chosen on top of the superellipsoid that best fits the discretized stellar surface $\mathcal{S}_{\rm NS}$. We have indeed verified that for largely deformed stars choosing collocation points on the discretized surface can excite high frequency numerical noise, that can compromise the accuracy with which high-ℓ coefficients are computed. Given the iterative nature of the algorithm, this might compromise the overall convergence. The equation of the superellipsoid in polar coordinates is given by

$$r = \left[\left(\frac{\cos\theta}{r_{\rm p}} \right)^{n_{\rm s}} + \left(\frac{\sin\theta}{r_{\rm eq}} \right)^{n_{\rm s}} \right]^{-\frac{1}{n_{\rm s}}}, \tag{56}$$

where $r_{\rm p}$ is the polar radius, $r_{\rm eq}$ is the equatorial radius and $n_{\rm s}$ regulates the shape of the ellipse. Interestingly in almost all cases $\mathcal{S}_{\rm NS}$ can be approximated by a superellipsoid with $1.5 \lesssim n_{\rm s} \lesssim 3$ with an error of at most one grid point ($\lesssim 1$ per cent). Once $\Phi_{\rm a}$ has been obtained, the potential Φ can be corrected in $\Phi_{\rm new} = \Phi - \Phi_{\rm a}$ to satisfy ideal MHD inside the star. As expected $\Phi_{\rm new}$ is now continuous but not differentiable across the surface.

Note that the ideal MHD condition (34), does not completely set the scalar potential $\Phi_{\rm new}$, which is still defined minus an arbitrary constant C. As pointed out by Bocquet et al. (1995), the constant C corresponds to an arbitrary charge, that can be added to the star. The value of C cannot be determined purely based on symmetric or equilibrium considerations, but only based on physical arguments. A common choice, often done in the literature, is to require that the NS is globally neutral, based on the physical argument that any charged body in space can attract charges from the surrounding to neutralize itself (Goldreich & Julian 1969; Bocquet et al. 1995; Franzon & Schramm 2015). This argument is however justified only for non-rotating systems. In the rotating case there is a clear ambiguity about which reference frame to consider. It is indeed well known that a neutrally charged rotating NS can easily pull charges

Downloaded from https://academic.oup.com/mnras/article-abstract/470/2/2469/3820933 by INAF Trieste (Osservatorio Astronomico di Trieste) user on 14 July 2020

from its surface, thus creating a magnetosphere and charging itself (Goldreich & Julian 1969).

Other different choices have been presented even if less often. One can assume a net charge, in order to minimize the electric field, responsible for the extraction of charges from the surface (Michel 1974), or in order to minimize the electromagnetic energy in the space outside the star (Ruffini & Treves 1973). All of these different choices lead to the same internal electromagnetic field giving the same deformation of the matter distribution inside the NS. They only differ in the structure of the external electric field, the surface charge, and the associated surface Lorentz force, as we will show.

In this work, we consider both neutrally charged NS, minimizing iteratively the monopolar content of $\Phi_{\rm new}$ with the same approach discussed in Bocquet et al. (1995), and electromagnetic configurations that minimize the polar Lorentz force. The latter case is realized by simply minimizing the discontinuity of the electric field at the pole.

Finally, it is evident from the discussion above, that also the magnetic flux Ψ is defined minus an harmonic term. In general, this degree of freedom has been neglected, leading to a smooth magnetic field. In principle, once one relaxes the requirement for a smooth electric field, covariance demands that a similar requirement should be relaxed for the magnetic field too: there is an arbitrary surface current that can only be fixed on physical arguments.

3.2 Algorithm and setup

The following points summarize the computational work-flow of the iterative procedure used in XNS:

(i) we start with an initial guess [the TOV solution at the beginning (Tolman 1939)];
(ii) the XCFC Einstein equations are solved for the metric functions;
(iii) the three-velocity v^{ϕ} and the Lorentz factor Γ are obtained on top of the new metric;
(iv) depending on the morphology for the magnetic field the Lorentz force contribution to the Bernoulli integral $\mathcal{M}$ is evaluated through different approaches:

(a) if the magnetic field configuration is purely toroidal the potential $\mathcal{M}$ is given by equation (47);
(b) in the case of a static configuration endowed with a poloidal magnetic field, the magnetic potential Ψ is obtained from equations (22) and (43), finally determining $\mathcal{M}$;
(c) if the magnetic field is purely poloidal but the star is rotating we iteratively solve together both the Maxwell–Gauss equation (21) and the Ampère equation (22) (respectively for the potentials Φ and Ψ), initializing the source terms using equation (44) and assuming vacuum outside the star;

(v) the Bernoulli integral is finally solved via a Newton method and the fluid quantities are updated in order to start a new iterative cycle;
(vi) steps from (ii) to (v) are repeated until convergence to a desired tolerance is achieved.

Numerical equilibrium configurations are obtained using 30 spherical harmonics on top of a uniform numerical grid in spherical coordinates covering the ranges $r = [0, 30]$ (in geometrized units) and $\theta = [0, \pi]$, with 600 points in the radial direction and 300 points in the azimuthal one. The radial domain has been chosen such that its outer boundary is far enough from the stellar surface so that the asymptotic behaviour of the different metric terms can be imposed properly. In some cases of strongly magnetized star with purely toroidal field, the outer boundary of the grid has been set to $r = 50$, in order to model also highly inflated configurations. The convergence tolerance is fixed to $\sim 10^{-8}$ (convergence is checked looking at the maximum deviation between successive solutions). Globally, we have verified that, because of the discretization errors, the overall accuracy of the final solutions is of the order of $\sim 10^{-3}$.

We want to remark here that the solutions to both Einstein and Maxwell equations are searched over the entire numerical grid without a matching conditions at the stellar surface, and this necessitates correcting the Φ potential in the case of rotating poloidal magnetized NSs. We found that the correction procedure described in the previous subsection can be realized with $N_\ell \sim 20$ in order to enforce equation (54) to discretization accuracy.

4 NUMERICAL RESULTS

In this section, we present a detailed investigation of the parameter space for the equilibrium configurations of rotating magnetized neutron endowed with either a purely toroidal or a purely poloidal magnetic field. Given that our focus is on the role of rotation and magnetic field in shaping the structure of the NS we considered just a simple polytropic EoS $p = K\rho^{1+1/n}$, with an adiabatic index $n = 1$ and a polytropic constant $K = 1.601 \times 10^5 {\rm cm}^5 {\rm g}^{-1} {\rm s}^{-2}$ (corresponding to $K_a = 110$ in geometrized units), in line with our previous work (PBD14). All stellar quantities (such as the gravitational mass M, the absolute value of the gravitational binding energy W, the surface ellipticity $e_{\rm s}$, the mean deformation $\bar{e}$ and so on) are defined as in Kiuchi & Yoshida (2008), Frieben & Rezzolla (2012) (hereafter FR12) and PBD14.

4.1 Toroidal magnetic field

In continuity with what has been done in PBD14 we have computed a large set of equilibria varying the central density, the magnetization, the magnetic field profile and the rotation frequency. The latter is however maintained below $\Omega = 5.08 \times 10^3 {\rm s}^{-1}$ (corresponding to $\Omega = 2.5 \times 10^{-2}$ in non-dimensional units). At this frequency the space of solutions is quite narrow due to mass shedding, mostly limited to very compact configurations, while less compact stars are more prone to magnetic and rotational deformation.

The parameter space is shown in Fig. 1, for $m = 1$ and different values of the rotational rate Ω. Models are given in terms of the central density ρ_c and the gravitational mass M. For each value of Ω we plot sequences of constant baryonic mass M_0 and of constant magnetic flux $\Phi_{\rm B}$, and sequences of constant deformation ratio $\bar{e}$ and fixed maximum magnetic field strength $B_{\rm max}$. Notice that at low central density the space of solutions is limited by two physical boundaries: the unmagnetized limit (red line) and the mass shedding limit (yellow line). Let us begin by discussing the general interplay between rotation and magnetic field. As already pointed out by FR12, depending on the strength of the magnetic field versus the rotation rate, we can obtain three main typologies of deformation, as shown in Fig. 2 and Table 1: if the rotation is dominant the resulting configuration is purely oblate with both positive surface ellipticity $e_{\rm s}$ and mean deformation rate $\bar{e}$ (left-hand panel of Fig. 2); conversely, if the effects due to the magnetic field prevail, the star is purely prolate with $\bar{e} < 0$ and $e_{\rm s} < 0$, or at most $e_{\rm s} = 0$ (central panel of Fig. 2); for intermediate configurations, when magnetization and rotation can counterbalance, the morphology of the star is only apparently oblate, with $e_{\rm s} > 0$, but globally prolate, with $\bar{e} < 0$ (right-hand panel of Fig. 2).

Downloaded from https://academic.oup.com/mnras/article-abstract/470/2/2469/3820933 by INAF Trieste (Osservatorio Astronomico di Trieste) user on 14 July 2020

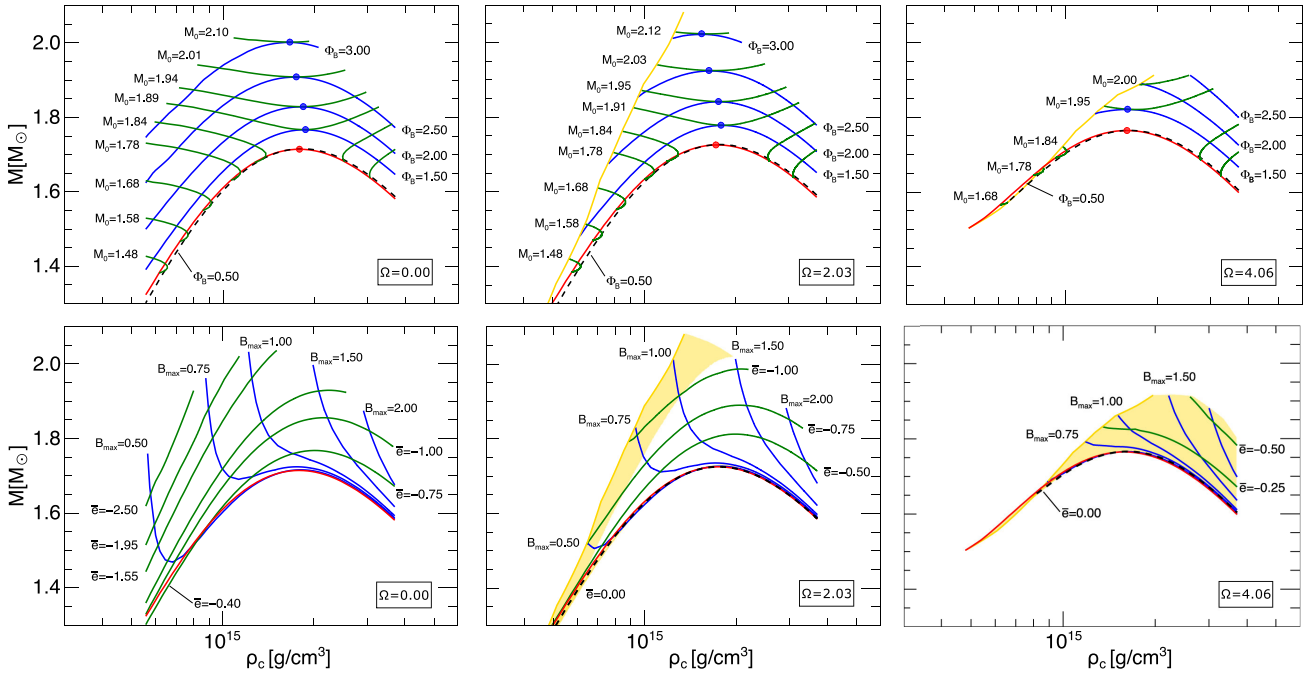

Figure 1. Space of physical solutions for magnetized NSs with magnetic index $m = 1$. Top row: equilibrium sequences with fixed baryonic mass M_0 (green lines) and fixed magnetic flux Φ_B (blue lines) for different values of the rotational rate Ω. The black dashed lines represent configurations with low value of the magnetic flux. Bottom row: equilibrium sequences at fixed maximum magnetic field strength B_{max} (blue lines) and fixed deformation rate $\bar{e}$. Here, the black dashed lines represent magnetized configurations with vanishing $\bar{e}$, while the yellow shaded regions correspond to those configurations having positive surface ellipticity. In all cases the red lines represent the unmagnetized sequences. The baryonic mass M_0 is expressed in unity of $M_\odot$, Φ_B in unity of 10^{30} G cm^2, B_{max} in unity of 10^{18} G and the rotational rate is expressed in 10^3 s^{-1}.

While rigid rotation flattens the star towards the equatorial plane (increases its *oblateness*), the Lorentz force squeezes the star in the direction of the magnetic axis inflating also the outer stellar layers (increases its *prolateness*). Moreover while the rotation acts mainly in the outer region, where the specific rotational energy is larger, the magnetic field affects mainly the inner regions where its strength peaks. As a result, close to mass shedding, the star shows a peculiar diamond-like shape. In general, the surface can be approximated by standard ellipsoids with n_s in the range 1.9–2.1. It is only for these peculiar diamond-shaped surfaces that the superellipsoid index lowers to ∼1.7.

As already discussed in PBD14 the gravitational mass of an equilibrium configuration generally grows with the magnetic flux Φ_B. This trend is reversed only in a small region of the parameter space characterized by weak magnetization ($\Phi_B \lesssim 5 \times 10^{29}$ G cm^2) and low central density ($\rho \lesssim 10^{15}$ g cm^{-3}), that is present also in the case of fast rotators. Moreover along sequences with fixed Φ_B, the configurations with the higher gravitational mass are very close to those having the higher value for the baryonic mass M_0 (they are coincident within the approximation of our code as can be seen in Fig. 1). These trends remain qualitatively unchanged also in the case of rotation. However, comparing the same sequences for different values of the rotational frequency Ω, it is clear that also the rotation contributes to increase both the gravitational and the baryonic mass. For example the maximum mass on the unmagnetized sequences $\Phi_B = 0$, changes from $M = 1.710 M_\odot$ in the non-rotating case to $M = 1.805 M_\odot$ for $\Omega = 5.3 \times 10^3$ s^{-1}, while the related central density drops by ∼30 per cent (and from $M = 1.770 M_\odot$ in the non-rotating case to $M = 1.820 M_\odot$ for $\Omega = 4.2 \times 10^3$ s^{-1} if $\Phi_B = 2.0 \times 10^{30}$ G cm^2). The increase of the gravitational and the baryonic mass, at a given central density, is a simple volume effect and it is mainly linked to the growth of the stellar radius caused by the rotation and the magnetic field. The magnetic energy and the rotational energy indeed contribute together to the value of the gravitational mass for at most few per cent.

The locus of points with $\bar{e} = 0$ is shown in the bottom panels of Fig. 1 as a black dashed line. Configurations that are found below this line, characterized by weaker magnetization, have $\bar{e} > 0$. In the same figure we also show the region of the parameter space where the equatorial radius of the star is larger than the polar one: $e_s > 0$. This yellow shaded region includes not only the purely oblate configurations with $\bar{e} > 0$ but also strongly magnetized equilibria located in proximity of the mass shedding limit. Notice that for rapid rotators with $\Omega \gtrsim 3 \times 10^3$s^{-1} almost all the obtained equilibria appear as oblate ellipsoids. Finally, at higher magnetization the mass shedding limit occurs at higher densities with respect to the non-magnetized case. This happens because the toroidal magnetic field significantly expands and rarefies the outer layers of the star making them volatile to centrifugal effects.

4.1.1 Results at fixed gravitational mass and magnetic polytropic index

We present in this subsection a detailed analysis of models at fixed gravitational mass, and fixed magnetic polytropic index m. For simplicity, and for consistency with previously published results (FR12; PBD14), we will focus on models with $M = 1.55 M_\odot$ and $m = 1$. We want to stress however that the results we found, from a qualitative point of view, apply also to cases with different m. Quantitative

Downloaded from https://academic.oup.com/mnras/article-abstract/470/2/2469/3820933 by INAF Trieste (Osservatorio Astronomico di Trieste) user on 14 July 2020

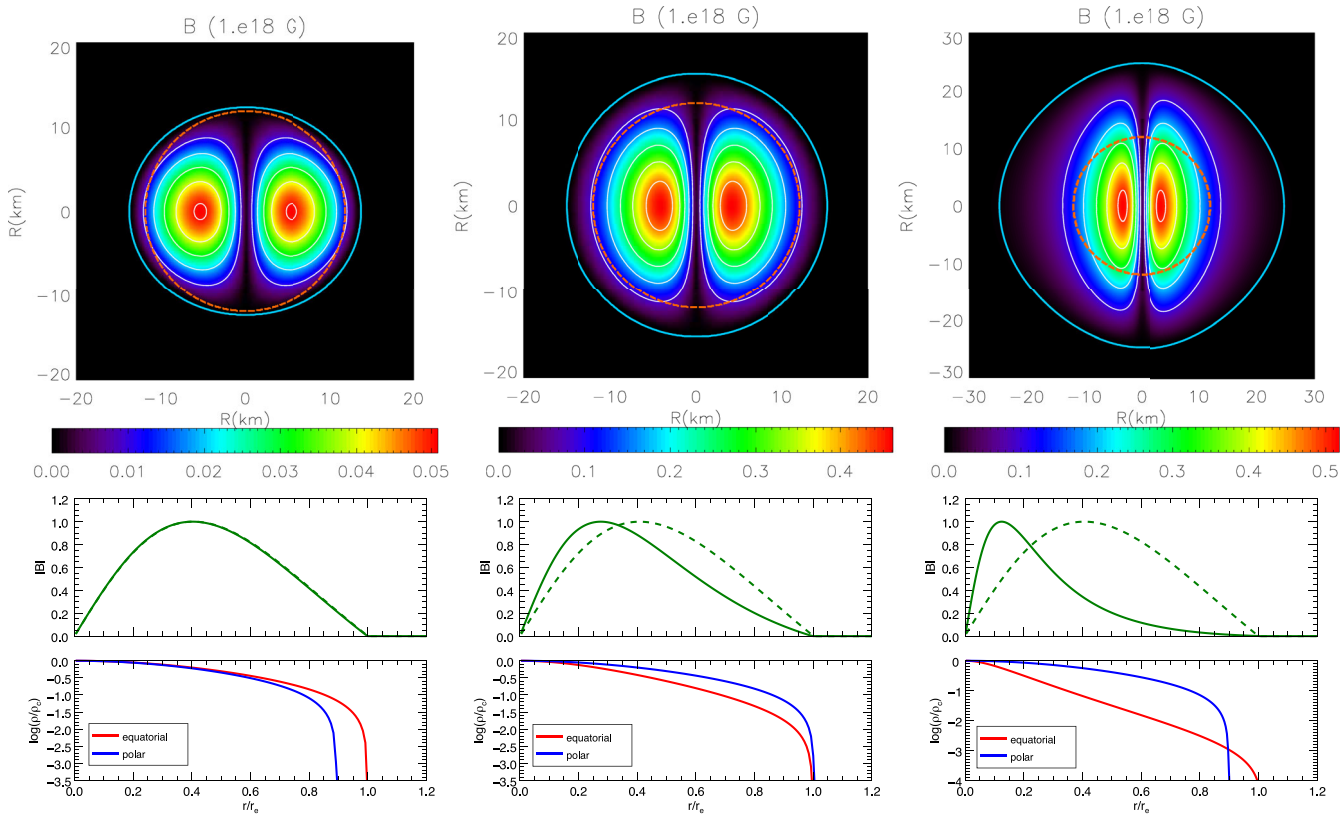

Figure 2. Top panels: distribution and isocontours of the magnetic field strength $B = \sqrt{B^{\phi} B_{\phi}}$ for equilibrium configurations with the same gravitational mass $M = 1.55\mathrm{M}_{\odot}$ but different rotational rate: $\Omega = 3.05 \times 10^3\ \mathrm{s}^{-1}$ (left-hand panel), $\Omega = 2.03 \times 10^3\ \mathrm{s}^{-1}$ (central and right-hand panel). The blue lines represent the stellar surface while the dashed lines represent the surface of the non-rotating and unmagnetized model with the same gravitational mass. Bottom panels: profiles of the magnetic field strength and of the baryon density normalized to the peak value along the equatorial direction $\theta = \pi/2$. The green dashed lines represent the magnetic field distribution in the weak magnetization limit ($B_{\max} \lesssim 10^{16}$ G). Radii are normalized to the equatorial radius r_{e}. Global physical quantities for these equilibrium configurations are listed in Table 1.

Table 1. Global quantities for the configuration shown in Fig. 2 with gravitational mass $M = 1.55\mathrm{M}_{\odot}$.

$B_{\max}$ 10^{17} G	Ω $10^3\ \mathrm{s}^{-1}$	ρ_{c} $10^{14}\mathrm{g\,cm}^{-3}$	M_0 $\mathrm{M}_{\odot}$	R_{circ} km	$r_{\mathrm{p}}/r_{\mathrm{e}}$	$\bar{e}$	n_{s}	H/W 10^{-1}	T/W 10^{-1}	H/M 10^{-2}	T/M 10^{-2}
0.51	3.05	7.31	1.67	15.6	0.90	0.09	2.00	0.01	0.25	0.02	3.81
4.63	2.03	8.24	1.66	16.9	1.00	−0.23	2.00	1.03	0.12	1.32	0.16
5.20	2.03	6.63	1.62	28.9	0.90	−0.79	1.76	2.30	0.19	2.44	0.21

differences with respect to the distribution of magnetic field will be discussed in the next subsection.

In analogy to what has been done in PBD14, to which we refer for a discussion on how deviations of the various quantities are defined, in Fig. 3 we show the variation of the central density ρ_{c}, of the baryonic mass M_0 and of the circumferential radius R_{c} as a function of $B_{\max}$ and for different values of Ω. As expected, as the rotational rate increases, the central density together with the baryonic mass drops, while the equatorial circumferential radius R_{c} expands.

Interestingly, the effect of the magnetic field along these equilibrium sequences is qualitatively independent from the specific value of Ω, tracing the same behaviours of static equilibria discussed in in PBD14: for small values of the magnetization parameter K_{m}, corresponding to $B_{\max} \lesssim 4 \times 10^{17}$G, the magnetic tension compresses the core of the star causing a growth in the central density ρ_{c}; at higher values of the magnetization the effect of the magnetic pressure becomes dominant and the outer layers of the star expand, while the central density starts to drop and the field strength reaches a maximum. The rotation acts in two ways: it produces an offset, which can be safely computed for unmagnetized models, and it increases the effectiveness of the magnetic field (at higher rotations a lower value of $B_{\max}$ is required to achieve the same deviation). Indeed we verified that the curves can be superimposed adding an offset corresponding to the unmagnetized rotators ($B_{\max} = 0$), and slightly rescaling the magnetic field with Ω. At higher rotation rate, when the unmagnetized star is already close to the *mass shedding limit*, the magnetic field can be increased only marginally, and the magnetic non-linear regime of highly inflated stars is never reached. We found that while at $\Omega = 2 \times 10^3 \mathrm{s}^{-1}$ the star reaches

Downloaded from https://academic.oup.com/mnras/article-abstract/470/2/2469/3820933 by INAF Trieste (Osservatorio Astronomico di Trieste) user on 14 July 2020

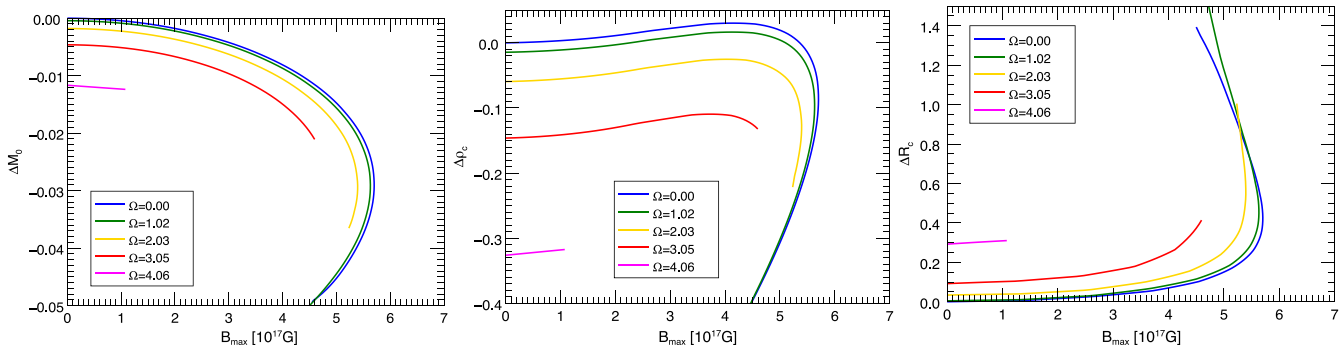

Figure 3. Variation with respect to the unmagnetized and non-rotating reference model of the baryon central density ρ_c, of the baryon mass M_0 and of the circumferential radius R_{circ} along the equilibrium sequences with fixed gravitational mass $M = 1.55\,M_\odot$, fixed magnetization index $m = 1$ but with different Ω expressed in unity of 10^3 s^{-1}.

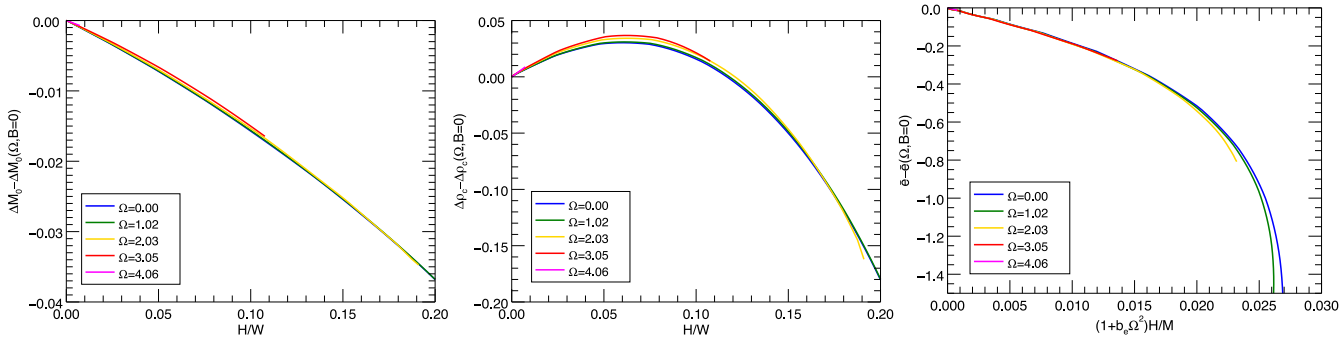

Figure 4. Variation of the baryonic mass, of the central density and of the deformation rate $\bar{e}$ with respect to the unmagnetized rotating reference model, as a function of the magnetic energy to binding energy ratio H/W or to gravitational mass H/M. The equilibrium sequences with different Ω are computed holding constant the gravitational mass $M = 1.55\,M_\odot$.

the mass shedding when $B_{max} = 5.1 \times 10^{17}$ G, and $H/M = 0.0245$, at $\Omega = 4 \times 10^3 s^{-1}$ this happens for $B_{max} = 1.1 \times 10^{17}$ G, and $H/M = 0.001$.

Another interesting parameter that describes the joint effect of magnetic field and rotation is the apparent ellipticity. We find that as the rotation rate increases, this shows a peculiar trend. At low magnetization, the surface shape is always oblate, as expected for an unmagnetized rotator. As the magnetic field increases, the oblateness diminishes and the shape can become prolate (this happens only for $\Omega < 2.5 \times 10^3 s^{-1}$). Then as the magnetic field begins to inflate the outer layer of the star, the local centrifugal support is enhanced, and the star becomes oblate again (we observe this already at $\Omega = 10^3 s^{-1}$). It was suggested by FR12 that at the mass shedding all models show apparent oblateness: $R_{eq} > R_{pol}$. This is consistent with our findings. For example models with $\Omega = 10^3 s^{-1}$ have $e_s = -0.02$ at mass shedding. At lower rotation rates the accuracy with which we sample the surface, does not allow us to draw any conclusion. However this second transition towards apparent oblateness, only takes place in a range of magnetic energy extremely close to the threshold for mass shedding, when the circumferential radius almost doubles its size.

The trends shown in Fig. 4 suggest that it should be possible to find how global quantities change with similarity variable, such as the energy ratios H/M and H/W. In the Newtonian case, in the limit $\Omega, B_{max} \to 0$, it can be shown that deviations should scale bilinearly in H/W and T/W (Cutler 2002). These ratios represent, in fact, the relative energies of terms leading to deformations (magnetic field and rotation) with respect to the gravitational binding energy that tends to sphericize the star. We find for example that quantities like the baryon mass variation ΔM_0, the change in central density $\Delta\rho_c$ or in circumferential radius ΔR_{circ}, and the deformation ratio $\bar{e}$ can be fitted at fixed M and m for all values of Ω and B_{max} as

$$\Delta q = \mathcal{G}_q(\Omega, H = 0) + \mathcal{F}_q \left([1 + a_q \Omega^2_{ms}] H/W \right), \quad (57)$$

where the subscript q stands for a generic stellar quantities, as shown in Fig. 4. Here, Ω_{ms} is the rotation rate in units of the frequency of a millisecond rotator. The function $\mathcal{F}$ is linear in H/W in the limit $H \to 0$, as expected, while a_q represents the non-linear coupling between magnetic field and rotation. This non-linear coupling term is small because rotation and magnetization cannot be increased independently in an arbitrary way, due to mass shedding. In the case of $\bar{e}$, we find $a_{\bar{e}} = -0.96$. Within this parametrization the role of rotation is completely factored out in $\mathcal{G}$ (even if the kinetic energy enters also in the definition of W), which is linear in Ω^2 in the limit $\Omega \to 0$. It is remarkable that this self-similar scaling holds for highly deformed star in the full GR regime.

Interestingly, the deformation $\bar{e}$ can be fitted equivalently in terms of H/M as

$$\bar{e} = \mathcal{G}_{\bar{e}}(\Omega, H = 0) + \mathcal{B}_{\bar{e}} \left([1 + b_{\bar{e}} \Omega^2_{ms}] H/M \right), \quad (58)$$

with $b_{\bar{e}} = -0.48$, as shown in Fig. 4. This reflects the fact that the non-linear coupling between rotation and magnetic field is negligible.

The bilinear approximation for the deformation is found to hold, with an error <10 per cent in the range $H/M \lesssim 0.01$, $T/M \lesssim 0.006$ (equivalently $H/W \lesssim 0.07$, $T/W \lesssim 0.04$ or $B_{max} \lesssim 4 \times 10^{17}$ G, $\Omega \lesssim 10^3 s^{-1}$), where one can write

$$\bar{e} \simeq -d_B B^2_{17} + d_\Omega \Omega^2_{ms}, \quad (59)$$

Downloaded from https://academic.oup.com/mnras/article-abstract/470/2/2469/3820933 by INAF Trieste (Osservatorio Astronomico di Trieste) user on 14 July 2020

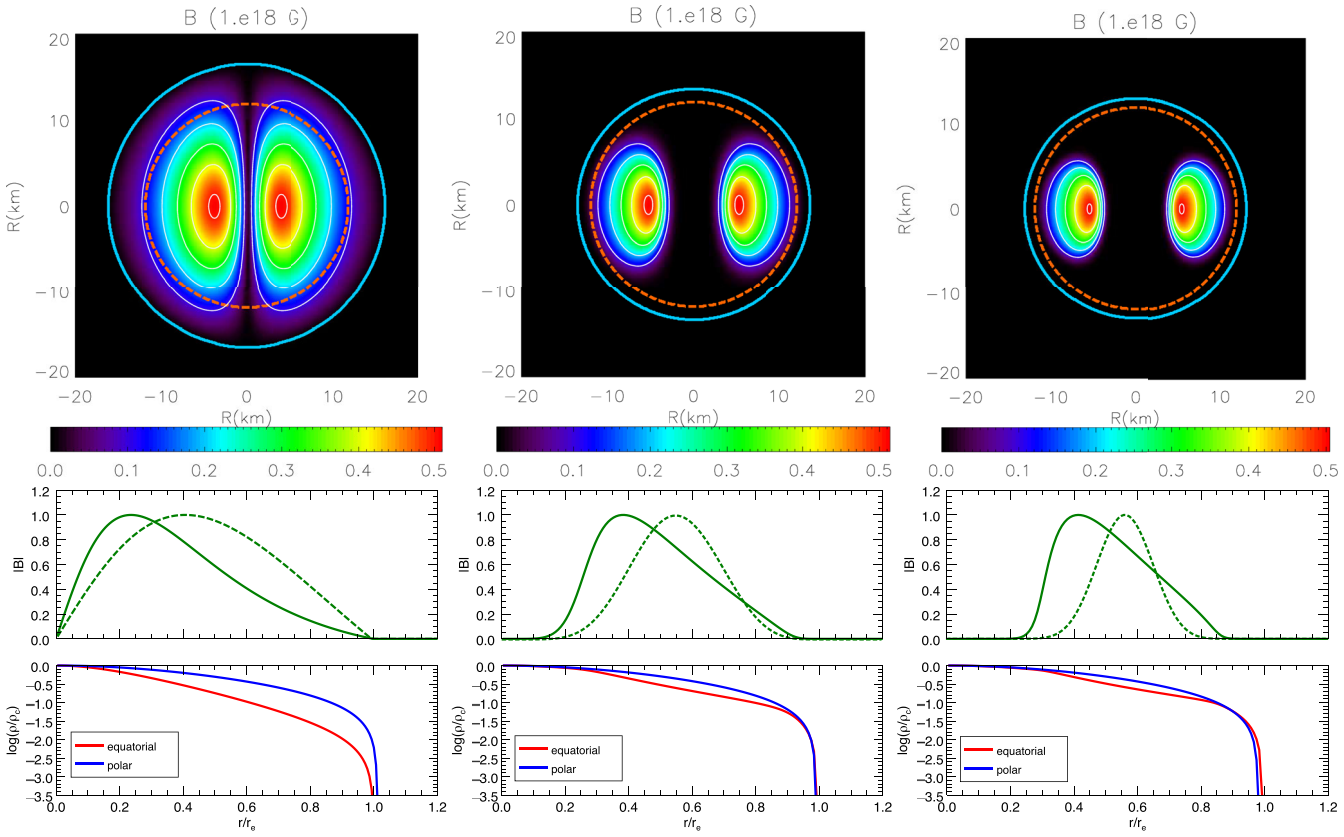

Figure 5. Top panels: distribution and isocontours of the magnetic field strength $B = \sqrt{B^{\phi} B_{\phi}}$ for equilibrium configurations with the same gravitational mass $M = 1.55 M_{\odot}$ and rotational rate $\Omega = 1.015 \times 10^3\ \mathrm{s}^{-1}$ but with different values of the magnetization index: $m = 1$ (left), $m = 4$ (middle) and $m = 10$ (right). The blue line is the stellar surface. Bottom panels: radial profiles of the magnetic field strength and of the baryon density normalized to peak values along the equatorial direction $\theta = \pi/2$ and the polar direction $\theta = 0$. The green dashed lines represent the magnetic field radial profile in the weak magnetization limit ($B_{\max} \lesssim 10^{16}$ G). Radii are normalized to the equatorial value r_{e}. Global physical quantities for these equilibrium configurations are listed in Table 2.

with $d_B \simeq 9 \times 10^{-3}$ and $d_{\Omega} \simeq 0.3$ (B_{17} is the maximum magnetic field strength in units 10^{17} G). In this linear regime the effects induced by rotation and magnetic field on the global deformation of the star $\bar{e}$ cancel if $B_{17} \simeq 6\,\Omega_{\mathrm{ms}}$, corresponding to $H/T \simeq 1.2$.

In the same limit Ω, $B_{\max} \to 0$, also the apparent ellipticity of the surface can be fitted with a similar bilinear dependence:

$$e_{\mathrm{S}} \simeq -s_{\mathrm{B}}\, B_{17}^2 + s_{\Omega}\, \Omega_{\mathrm{ms}}^2, \tag{60}$$

with $s_{\mathrm{B}} \simeq 2.5 \times 10^{-3}$ and $s_{\Omega} \simeq 0.4$. Notice that, concerning the apparent ellipticity, the effects induced by rotation and magnetic field cancel at $B_{17} \simeq 13\,\Omega_{\mathrm{ms}}$, corresponding to a ratio of magnetic to kinetic energy $H/T \simeq 6.8$. This is about a factor 5 higher than for $\bar{e}$, indicating that apparently oblate stars can have a matter distribution with a net prolate quadrupole.

It is evident that in terms of quadrupolar deformation, the contribution of the magnetic energy is analogous (even if acting in the opposite way) to that of the rotational energy, and the two tend to compensate each other close to equipartition, while rotational energy is slightly more efficient in determining the shape of the surface. This because magnetic field tends to act in the interior, while rotation mostly affects the outer layers. Note that while formally a parametrization in terms of Ω^2 and $B_{\max}^2$ is equivalent to one in T and H, the latter holds with the same accuracy for a ∼50 per cent larger range of magnetic field strengths and rotation rates.

4.1.2 The role of magnetic field distribution at fixed gravitational mass

Let us now discuss the effects of different magnetic field distributions parametrized by the magnetization index m. A comparison in the non-rotating case was already presented in PBD14. Here some of the results are reviewed in view of the trends found in the previous subsection. We recall that the self-similarity scalings found previously apply also to other values of m.

In Fig. 5, we show a comparison among equilibria with the same gravitational mass and the same value of the maximum magnetic field strength but with different values of m. A quantitative characterization of these configurations is given in Table 2.

As the value of m increases the magnetic field distribution concentrates towards the surface of the star, with a larger fraction of the star that behaves as if it was essentially unmagnetized. As a consequence the magnetic energy (at fixed $B_{\max}$) is smaller. This effect however is progressively less pronounced at higher magnetization, as shown by the comparison with the perturbative regime in Fig. 5, where we plot the magnetic field distribution in the radial direction at the equator for both the strong and weak field regime.[2]

[2] Here and in the remainder of this paper we refer to *weak field regime* as the regime where the effects induced by the magnetic field on the NS can be safely computed adopting a perturbative approach. In the explored parameter space, this weak magnetization limit applies as long as $B_{\max} \lesssim 10^{16}$ G (see also Pili et al. 2015 or BPD15 for a discussion).

Downloaded from https://academic.oup.com/mnras/article-abstract/470/2/2469/3820933 by INAF Trieste (Osservatorio Astronomico di Trieste) user on 14 July 2020

Table 2. Global quantities for the configuration shown in Fig. 5 with gravitational mass $M = 1.55\mathrm{M}_\odot$ and rotation frequency $\Omega = 2.03 \times 10^3\ \mathrm{s}^{-1}$.

	$B_{\max}$ 10^{17} G	Ω $10^3\ \mathrm{s}^{-1}$	ρ_c $10^{14}\,\mathrm{g\,cm}^{-3}$	M_0 $\mathrm{M}_\odot$	$R_{\rm circ}$ km	r_p/r_e	$\bar{e}$	n_s	H/W 10^{-2}	T/W 10^{-2}	H/M 10^{-2}	T/M 10^{-3}
$m=1$	5.12	2.03	8.07	1.65	18.3	1.01	−0.35	2.00	12.3	1.16	1.76	1.58
$m=2$	5.15	2.03	7.93	1.66	16.2	1.01	−0.20	2.00	9.00	1.10	1.29	1.50
$m=4$	5.15	2.03	7.95	1.66	15.6	1.03	−0.12	2.00	6.65	1.05	0.98	1.55
$m=10$	5.07	2.03	7.98	1.67	15.3	1.03	−0.07	2.00	4.81	1.03	0.72	1.55

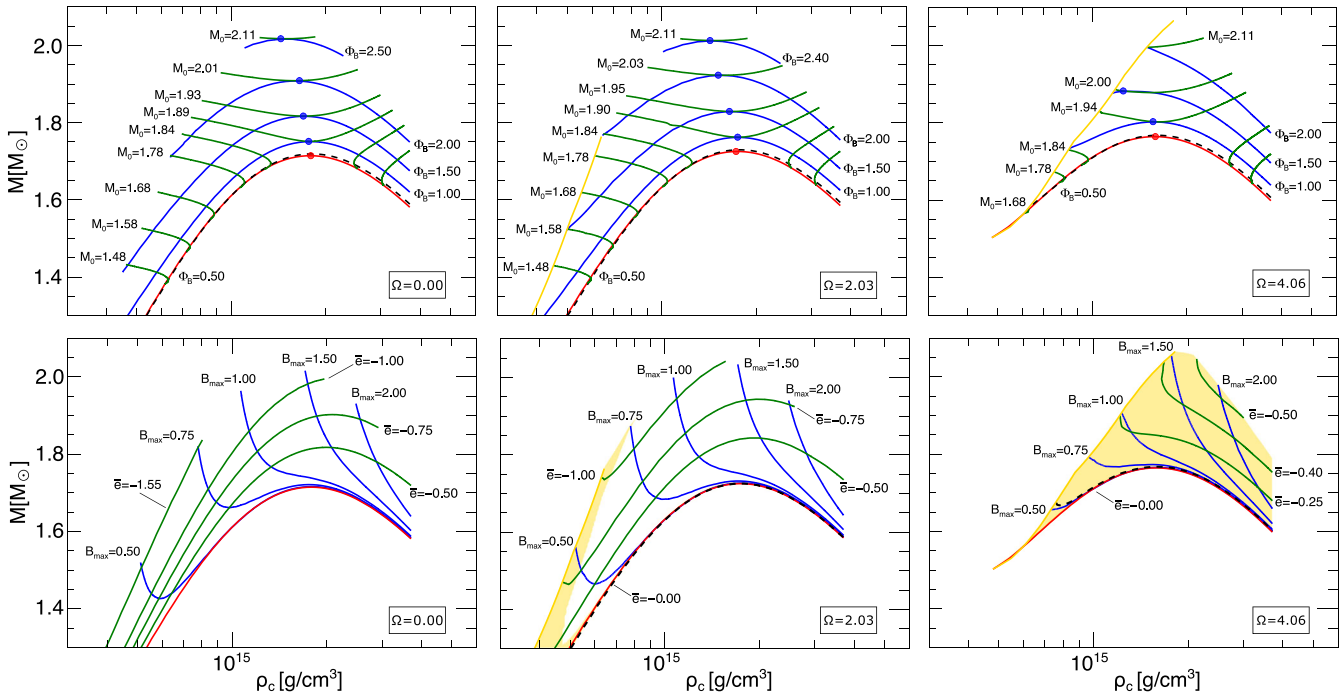

Figure 6. Space of physical solutions for magnetized NSs with magnetic index $m = 2$ and rigid rotation. Top row: equilibrium sequences with fixed baryonic mass M_0 (green lines) and fixed magnetic flux Φ_B (blue lines) for different values of the rotational rate Ω. The black dashed lines represent configurations with a low value of the magnetic flux. Bottom row: equilibrium sequences at fixed maximum magnetic field strength $B_{\max}$ (blue lines) and fixed deformation rate $\bar{e}$. Here the black dashed line represents magnetized configurations with $\bar{e} = 0$. The yellow shaded regions indicate those configurations having $e_s > 0$. The red lines represent the unmagnetized sequences. The baryonic mass M_0 is expressed in unity of $\mathrm{M}_\odot$, Φ_B in unity of $10^{30}\,\mathrm{G\,cm}^2$ and $B_{\max}$ in unity of 10^{18} G.

Hence, if parametrized in terms of the magnetic field strength, the effects of the magnetic field against rotation is strongly reduced at higher m, leading to smaller deformations and ellipticities. This is also evident from Fig. 6 where we plot the space of physical solutions in the case $m = 2$. Indeed, with respect to the $m = 1$ case (see Fig. 1), the mass-shedding line moves to lower densities and the region characterized by $e_s > 0$ shrinks towards models with lower compactness. In good part this is due to the fact that the inflationary effect on the outer layers of the star is also suppressed. In Fig. 7, we compare the trends of $\bar{e}$, along our usual equilibrium sequences with $M = 1.551\mathrm{M}_\odot$, considering cases with $m = 1$, 2, 4. It is evident that in terms of $B_{\max}$, the various cases show clearly distinct trends. However once parametrized in terms of H/W, the dependence on m for the baryonic mass ΔM_0 becomes negligible (less than at most 5 per cent for the fastest rotating configurations). In the case of $\bar{e}$ the parametrization in equation (57) leaves a residual dependence on m which is at most 15 per cent. This can be however reabsorbed defining an effective energy ratio:

$$\bar{e} = \mathcal{G}_{\bar{e}}(\Omega, H=0) + \mathcal{F}_{\bar{e}}\left(\left[1 + a_{\bar{e}}\Omega^2_{\rm ms}\right]\left[0.84 + \frac{0.16}{m}\right]\frac{H}{W}\right), \quad (61)$$

which now generalizes equation (57) for different magnetic field distributions. The same holds for the apparent ellipticity, with major differences arising only close to the saturation fields, $B_{\max} \gtrsim 4 \times 10^{17}$ G. Interestingly we found that, once parametrized in terms of H/M as in equation (58), both $\bar{e}$ and e_S show only a weak dependence (within 5 per cent) on the parameter m even in the non-linear phase (see Fig. 7). Moreover from an observational point of view, one may prefer a parametrization in terms of the gravitational mass which is indeed a measurable quantity.

In the bilinear regime, the parametrization given by equations (59) and (60), of the mean deformation $\bar{e}$ and of the surface ellipticity e_s, can be generalized as

$$\bar{e} \simeq -\frac{d_B}{m} B^2_{17} + d_\Omega\, \Omega^2_{\rm ms}, \quad (62)$$

$$e_s \simeq -\frac{s_B}{m} B^2_{17} + s_\Omega\, \Omega^2_{\rm ms}. \quad (63)$$

Now, since in the bilinear regime $\bar{e} \propto 17 H/M$, equation (62) also implies that $B_{17} = 42\sqrt{m\,H/M}$.

Given the small residual effect due to m, it is reasonable to conclude that the quadrupolar and surface deformation give only a direct indication of the magnetic energy content rather than of the

Downloaded from https://academic.oup.com/mnras/article-abstract/470/2/2469/3820933 by INAF Trieste (Osservatorio Astronomico di Trieste) user on 14 July 2020

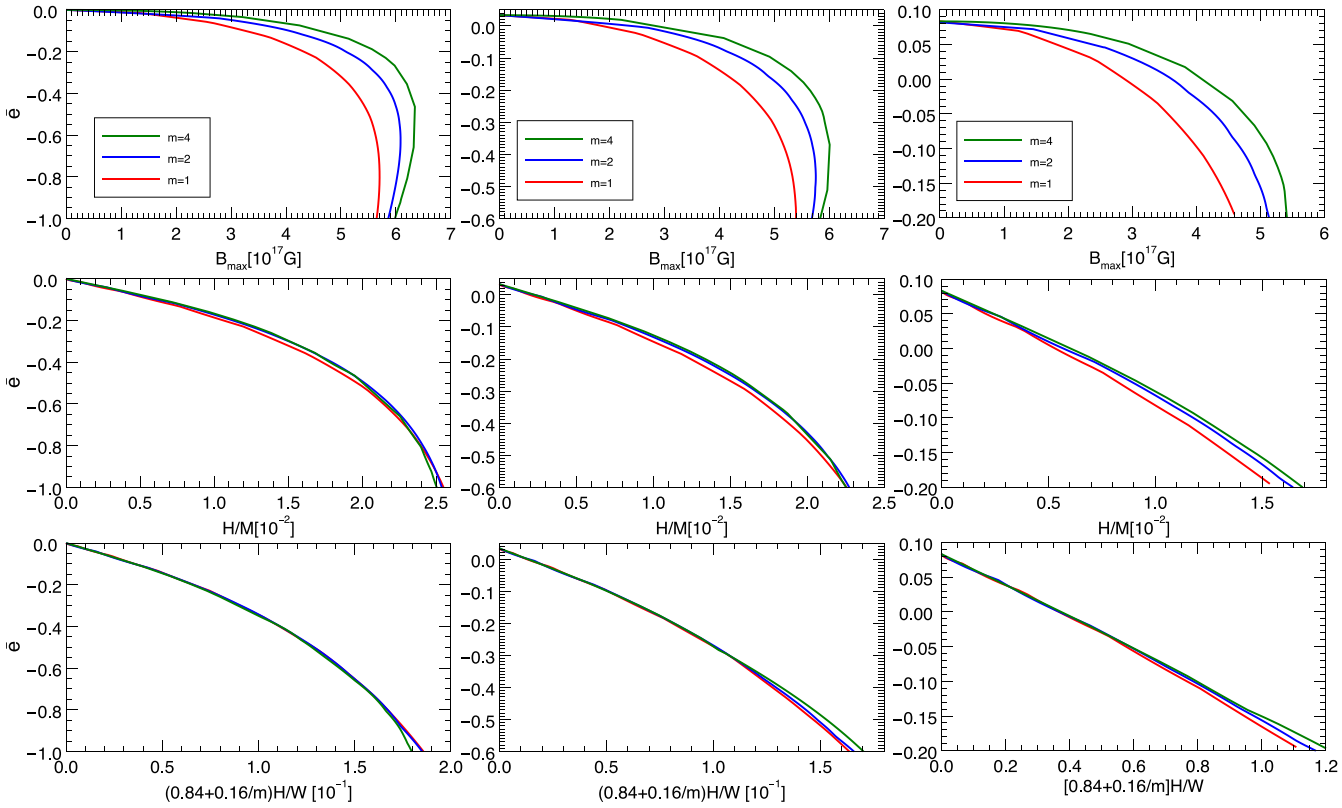

Figure 7. Mean deformation rate $\bar{e}$ as a function of the maximum magnetic field strength (top), of the magnetic energy to gravitational mass ratio (middle) and of the effective magnetic energy ratio $[H/W]_{\rm eff}$ for different values of the magnetization index $m \in \{1, 2, 4\}$ along sequences of fixed gravitational mass $M = 1.55\,{\rm M}_\odot$ in the static case (left), with $\Omega = 2.03 \times 10^3 {\rm s}^{-1}$ (centre) and $\Omega = 3.05 \times 10^3 {\rm s}^{-1}$ (right).

current distribution, at least in the case of purely toroidal magnetic fields.

4.1.3 *Trends at different mass*

Let us finish our discussion of models with toroidal magnetic field, by analysing how results change at different masses. In general, we found that the trends and scalings found in the previous sections still hold at different masses in stable branches of the mass density relation. Obviously at lower gravitational mass (corresponding also to a lower compactness) the effect of rotation and magnetic field are enhanced.

For the deformation ratio $\bar{e}$, in the case of unmagnetized rotators, it is possible to reabsorb the mass differences in the term due to rotation by using T/W, instead of Ω^2 or T/M. We also found that the trend is linear in T/W almost all the way up to the fastest rotators. Concerning the effects of the magnetic field on $\bar{e}$ and $e_{\rm S}$, we find that they can be rescaled defining an effective normalized (with respect to our fiducial model with $M = 1.55{\rm M}_\odot$) magnetic energy ratio and rotational coupling term, such that

$$\left[\frac{H}{W}\right]_{\rm eff} = \left[0.84 + \frac{0.16}{m}\right] \frac{1.55\,{\rm M}_\odot}{M} \frac{H}{W}, \tag{64}$$

$$a_{\bar{e}\,{\rm eff}} = -\left(3.94 - 2.98 \frac{M}{1.55\,{\rm M}_\odot}\right). \tag{65}$$

This behaviour was already found to hold in the linear regime at fixed mass and for different EoS by FR12. Here, we show that it can be also generalized for different masses and magnetic field distributions. Notice that, while the effects due to rotation scales as T/W, the magnetization effects go as H/WM. This might be related to the way mass stratification couples with rotation and magnetic field: for a rigid rotator, the rotational stratification is independent of density and mass; on the contrary, assuming the magnetic barotropic law equation (47), as mass and stratification change so does the magnetic field distribution. We find that the following functional form:

$$\bar{e} \simeq 3.2 \frac{T}{W}\bigg|_{B=0} + \mathcal{F}\left(\left[1 + a_{\bar{e},{\rm eff}}\Omega^2_{\rm ms}\right]\left[\frac{H}{W}\right]_{\rm eff}\right)$$
$$\text{with} \quad \mathcal{F}(x) = -2.71x - 0.068(10x)^{3.2} \tag{66}$$

fits the deformation ratio for all values of Ω, H, M and m up to $\bar{e} \simeq 1$, with an error less than 5 per cent as shown in Fig. 8.

Focusing on the bilinear regime, it is natural to expects that the coefficients in equation (62) are functions of mass. As shown in Table 3 both d_Ω and $d_{\rm B}$ are decreasing functions of M, while their ratio $d_\Omega/d_{\rm B}$ grows with M.

In this regime we can also simply equation (66) evaluating its limit as $H, T \to 0$, for which $W \to W_0 = {\rm const}$, so that

$$\bar{e} \simeq \frac{C_{\bar{e}}}{W_0}\left[T - 1.3\frac{H}{M/{\rm M}_\odot}\right], \tag{67}$$

where the coefficient $C_{\bar{e}}$ depends on the specific EoS and the mass of the reference unmagnetized stationary configuration: for our fiducial model with $M = 1.551\,{\rm M}_\odot$ we have $C_{\bar{e}} = 3.2$ and $W_0 = 0.25{\rm M}_\odot$. We recall that even the coefficient 1.3 in general has a residual dependence on m, but it can be taken as constant with an accuracy $\sim$10 per cent. We can conclude that, in the perturbative regime, the deformation ratio is linear in the quantity $T - 1.3H/(M/{\rm M}_\odot)$,

Downloaded from https://academic.oup.com/mnras/article-abstract/470/2/2469/3820933 by INAF Trieste (Osservatorio Astronomico di Trieste) user on 14 July 2020

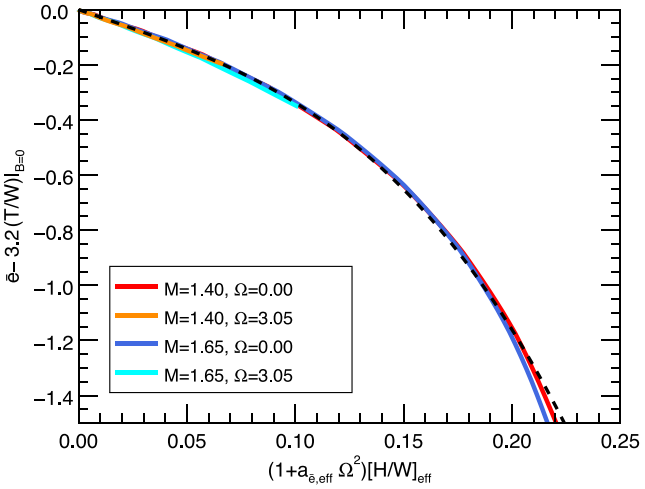

Figure 8. Deformation ratio $\bar{e}$ with respect to the unmagnetized model in terms of the effective magnetic energy ratio $[H/W]_{\rm eff}$ for configurations having gravitational mass 1.40–1.65 $M_\odot$ and rotational frequency $\Omega = 0.0$–3.05×10^3 s^{-1}. The black dashed line represents equation (66).

Table 3. Mass dependence for the $\bar{e}$ expansion coefficients in equation (62).

M $M_\odot$	W_0 $M_\odot$	d_Ω 10^{-1}	$d_{\rm B}$ 10^{-3}	s_Ω 10^{-1}	$s_{\rm B}$ 10^{-3}
1.40	0.18	4.5	15	6.0	4.8
1.45	0.20	4.0	13	5.1	4.1
1.50	0.23	3.6	11	4.6	3.6
1.55	0.25	3.1	9.5	3.8	2.6
1.60	0.28	2.8	7.0	3.5	2.2
1.65	0.32	2.3	5.5	3.1	1.5

which can be considered as a self-similarity variable, with all the information about the EoS, factored out in a single proportionality coefficient.

Repeating the same analysis for the surface deformation in the bilinear regime, we found that the coefficients $s_{\rm B}$ and s_Ω in equation (63) show analogous trends with those found for the deformation ratio. Coefficients are given in Table 3. Obviously a parametrization in terms of Ω^2 and $B^2_{\rm max}$ is not optimal, once different masses are taken into consideration (at fixed mass $\Omega^2 \propto T$ and $B^2_{\rm max} \propto H$, so it is equivalent to a parametrization in terms of kinetic and magnetic energies). We found that using the effective magnetic energy defined by equation (64), and T/W for the rotational contribution, the mass dependence can be reabsorbed analogously to equation (67), with an accuracy $\lesssim 10$ per cent

$$e_{\rm S} \simeq \frac{C_{e_{\rm s}}}{W_0}\left[T - 0.23\frac{H}{M/{\rm M}_\odot}\right], \qquad (68)$$

with $C_{e_{\rm s}} \sim 4.2$. Note that given the accuracy of our solution, the surface deformation of our models cannot be determined better than 0.01, and models with $e_{\rm S} \gtrsim 0.05$ are already in the non-linear regime.

In the case $M = 1.40{\rm M}_\odot$, we can compare our results to those obtained by Cutler (2002) and FR12. In the Newtonian regime they both provide the distortion coefficients for the parametrization $\bar{e} = a_\Omega T/W + a_{\rm B} H/W$: FR12 obtain $a_\Omega = 3.8$ and $a_{\rm B} = 3.5$, Cutler (2002) instead has $a_\Omega = a_{\rm B} = 3.75$. Differences between distortion coefficients depends on the choices for the EoS: both Cutler (2002) and FR12 adopt a NS having stellar radius $R = 10$ km as reference model but while the former adopt an incompressible fluid, the latter

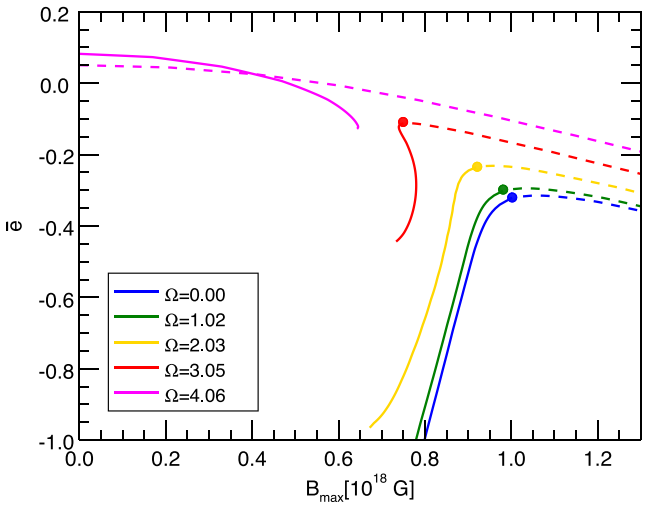

Figure 9. Variation of the mean deformation ratio $\bar{e}$ along equilibrium sequences characterized by fixed gravitational mass $M = 1.75{\rm M}_\odot$ and different value of Ω with $m = 1$. Filled circles represent the configurations with highest M_0 and they split each sequence into a low $\rho_{\rm c}$ (solid lines) and high $\rho_{\rm c}$ (dashed lines) branch.

a polytropic with $n = 1$. In our case we use $n = 1$ as well, but with a different polytropic constant leading to a NS with $R_{\rm circ} = 15$ km and we obtain $a_\Omega = 3.2$ and $a_{\rm B} = 2.97$ [see equation (67)]. Leading to less compact configurations, our choice should in principle imply higher value for a_Ω and $a_{\rm B}$. However our calculations are made within GR and as pointed out by FR12, a Newtonian treatment overestimates the correct distortion coefficients. Interestingly for $M = 1.4{\rm M}_\odot$, we find a ratio $a_\Omega/a_{\rm B} \sim 1.078$, similar to the value 1.085 found by FR12 in the Newtonian limit. This may suggest that the relative contributions of the magnetic field and of the rotation are the same independently from the compactness of the star that may only affect their absolute values.

A comparison in full GR is only possible with FR12 (see also PBD14), where however they adopt different parametrizations with respect to ours. In particular they express both the surface ellipticity $e_{\rm s}$ and the quadrupole deformation $e_{\rm q}$ using the average magnetic field strength $<B^2>$ instead of its maximum value $B^2_{\rm max}$:

$$e_{\rm s} = -b_{\rm B} <B^2_{15}> + b_\Omega\,\Omega^2, \quad e_q = -c_{\rm B} <B^2_{15}> + c_\Omega\,\Omega^2, \qquad (69)$$

where the magnetic field is normalized to 10^{15} G and Ω is expressed in s^{-1} (to be compared with our equations 63 and 62). Considering again their reference model at $M = 1.40\,{\rm M}_\odot$ and $m = 1$, we find that $<B^2> \sim 0.25 B^2_{\rm max}$ while $e_{\rm q} \simeq 0.5\bar{e}$ (see also Pili et al. 2015). Hence, the coefficients given in Table 3 translate into $b_{\rm B} = 1.9 \times 10^{-6}$, $b_\Omega = 1.5 \times 10^{-8}$ and $c_{\rm B} = 2.9 \times 10^{-6}$, $c_\Omega = 5.7 \times 10^{-8}$ in good agreement with FR12 considering $R_{\rm circ} \simeq$ 15km (see fig.13 of their paper).

In this section, we consider just equilibrium sequences with gravitational mass below the maximum mass of the static and unmagnetized sequences (i.e. $1.72{\rm M}_\odot$ for our choice of EoS) and central density $\rho_{\rm c} < 1.8 \times 10^{15}{\rm gcm}^{-3}$. This corresponds to selecting sequences that are connected to the stable unmagnetized static branch and for which a comparison with a static unmagnetized reference model is meaningful.

Trends become more complex if one considers supramassive sequences (see Kiuchi & Yoshida 2008 for discussion). An example is shown in Fig. 9 where we plot $\bar{e}$ as a function of Ω and $B_{\rm max}$ considering $M = 1.75\,{\rm M}_\odot$. Notice that with such gravitational mass,

Downloaded from https://academic.oup.com/mnras/article-abstract/470/2/2469/3820933 by INAF Trieste (Osservatorio Astronomico di Trieste) user on 14 July 2020

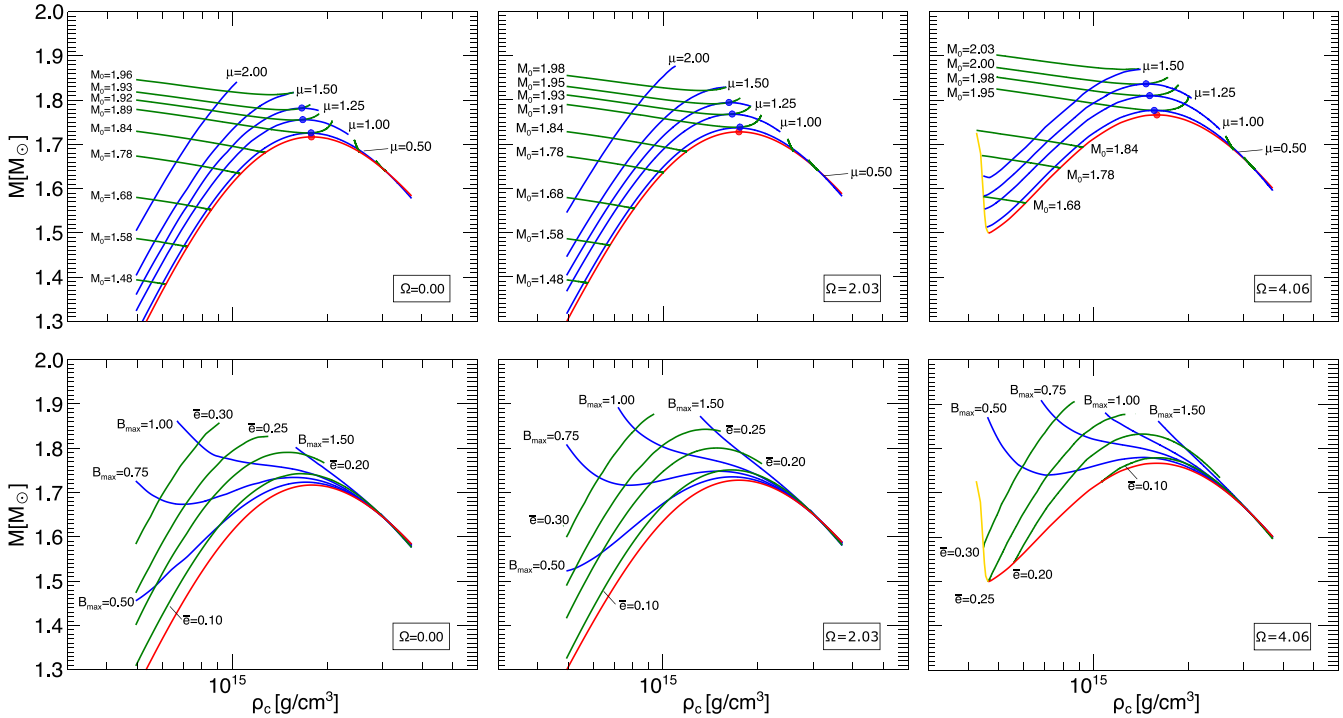

Figure 10. Space of physical solutions for rigidly rotating NSs endowed with purely poloidal magnetic field, obtained assuming a current distribution with $\xi = 0$ in equation (44). Top row: equilibrium sequences with fixed baryonic mass M_0 (green lines) and fixed magnetic dipole moment μ (blue lines). Bottom row: equilibrium sequences with fixed matter deformation $\bar{e}$ (green lines) or with fixed maximum magnetic strength $B_{\rm max}$ (blue lines). The yellow lines trace the mass shedding limit, while the red lines represent unmagnetized equilibria. The baryonic mass is expressed in units of $M_\odot$, μ is expressed in units of 10^{35}ergG^{-1}, $B_{\rm max}$ is expressed in units of 10^{18} G and finally the rotational rate Ω is in units of 10^3 s^{-1}.

no static configuration exists if $\Phi_{\rm B} < 1.31 \times 10^{30}$Gcm^2, neither unmagnetized configurations with $\Omega \lesssim 4 \times 10^3$s^{-1}. The behaviour of $\bar{e}$ in this case can be understood by looking also at Fig. 1. The configurations with the minimal deformation are very close to the ones that, at fixed gravitational mass, have the highest M_0. Moving away from this configuration, either towards lower or higher central densities, the absolute value of the deformation rises. At lower densities, despite the fact that the magnetic field also diminishes, the deformation rises because the star becomes less compact. At higher density, despite the star becoming more compact, the magnetic field rises and its effect on the deformation becomes stronger. As one can see the interplay between the magnetic field and the compactness can be quite different depending on the branch in the mass density sequence. For $\Omega \gtrsim 4 \times 10^3$s^{-1}, two unmagnetized configurations become possible (one stable one unstable) and the $\bar{e}$ sequence splits in two separated branches: the one connected with the unmagnetized configuration with lower $\rho_{\rm c}$, the other connected with the unmagnetized configuration with higher $\rho_{\rm c}$. Being this latter more compact, both the effect of rotation and of magnetic field are less pronounced.

4.2 Poloidal magnetic field

In this section, we will characterize the effects of a poloidal magnetic field, focusing on the simplest choice with $\xi = 0$ (see equation 44) and with a vanishing net charge. Our investigation is again limited to $\Omega \lesssim 5.1 \times 10^3$s^{-1} since at this frequency and for our choice of the EoS the parameter space is substantially reduced due to mass shedding.

The parameter space is shown in Fig. 10 in the $\rho_{\rm c}$–M plane for slices with fixed Ω. In line with PBD14, in each plot we show equilibrium sequences at fixed baryonic mass M_0, magnetic dipole moment μ, maximum field strength $B_{\rm max}$ or deformation $\bar{e}$. As expected, in analogy with the toroidal case, both the gravitational and baryon mass rise with the magnetization (or equivalently with the magnetic dipole moment μ) and with the rotational frequency Ω. Here, however, the magnetic field acts in the same way of the centrifugal force, flattening the star in the direction of the equatorial plane. As a consequence all the configurations are oblate and the surface ellipticity $e_{\rm s}$ is always positive. Differences between the two effects are only evident in the low-density region ($\rho_{\rm c} \lesssim 5 \times 10^{15}$g cm^{-3}). Indeed, although the majority of the stellar surfaces can be well approximated with standard ellipsoids having $n_{\rm s} \sim 2$, at low density the superellipsoid index ranges from $\sim$1.6, for the configuration at the mass-shedding limit, to $\eta \sim 2.8$ for the most magnetized NSs with $B_{\rm max} \gtrsim 7 \times 10^{17}$G: while rigid rotation acts preferentially on the external equatorial layers of the star, originating hypoellipsoidal with $n_{\rm s} < 2$, the Lorentz force associated with the poloidal magnetic field globally flattens the star, from the core to the external layers, reducing the polar radius and favouring the occurrence of hyperellipsoids with $n_{\rm s} > 2$. Two representative equilibrium configurations are shown in Fig. 11 and Table 4. They both share the same value of the gravitational mass but, because of the different degree of magnetization and rotation rate, they have $n_{\rm s} \sim 2.5$ (left-hand panel) and $n_{\rm s} \sim 1.8$ (right-hand panel). Notice that, even if the equatorial radius grows, the poloidal field does not inflate the outer layers of the star. As a consequence, the central density at mass shedding for a given Ω remains almost the same with respect to the unmagnetized case, as shown in the right-hand panels of Fig. 10. Our findings suggest that the poloidal field enhances the stability against the Keplerian limit: the equatorial Lorentz force points outward in the inner region of the star causing its

Downloaded from https://academic.oup.com/mnras/article-abstract/470/2/2469/3820933 by INAF Trieste (Osservatorio Astronomico di Trieste) user on 14 July 2020

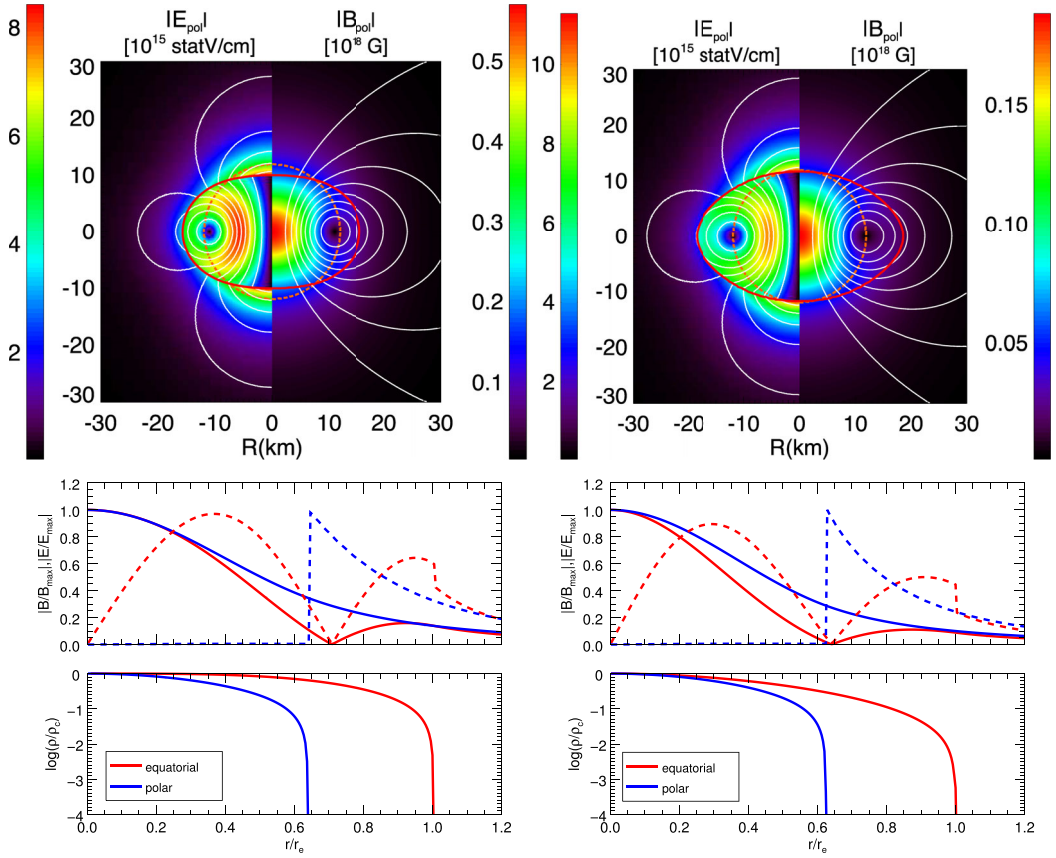

Figure 11. Top row: electric (left half panel) and magnetic (right half panel) field distribution together with the contours of the electric potential Φ (left half panel) and of the magnetic potential Ψ (right half panel) for two configurations sharing the same gravitational mass but with different $B_{\rm max}$ and Ω ($B_{\rm max} = 5.72 \times 10^{17}$ G and $\Omega = 1.02 \times 10^3 {\rm s}^{-1}$ for the configuration on the left, $B_{\rm max} = 1.88 \times 10^{17}$ G and $\Omega = 4.06 \times 10^3 {\rm s}^{-1}$ for the configuration on the right). Numerical details are shown in Table 4. Middle row: profile of the magnetic field strength (solid lines) and of the electric field strength (dashed lines) in the equatorial (red lines) and polar (blue lines) direction. Bottom rows: polar and equatorial radial profiles of the baryon density $\rho_{\rm c}$.

Table 4. Global quantities for the configuration shown in Fig. 11 with gravitational mass $M = 1.55{\rm M}_\odot$.

$B_{\rm max}$ 10^{17} G	Ω 10^3 s^{-1}	$\rho_{\rm c}$ 10^{14} g cm^{-3}	M_0 M$_\odot$	$R_{\rm circ}$ km	$r_{\rm p}/R_{\rm e}$	$\bar{e}$	$n_{\rm s}$	H/W 10^{-2}	T/W 10^{-2}	H/M 10^{-2}	T/M 10^{-2}
1.88	4.06	4.79	1.65	20.7	0.62	0.27	1.80	1.60	8.67	0.19	1.02
5.72	1.02	4.30	1.64	17.7	0.64	0.32	2.20	14.0	0.49	1.79	0.06

deformations, but points inward in the outer layers playing a confining role.

At very high magnetization, the internal structure of the NS changes dramatically since the magnetic force can evacuate the core so that the density reaches its maximum in a ring located in the equatorial plane rather than at the centre (see fig. 6 in PBD14). Because our numerical scheme is less accurate in this regime, in the present analysis we will exclude such kind of configurations. Moreover, as pointed out by Cardall et al. (2001), at even higher magnetization no stationary solution can be found because the magnetic field pushes off-centre a sufficient amount of mass that the gravitational force, near the centre of the star, points outward.

In Fig. 11, we show the morphology of the magnetic and electric field strength together with the isocontours of the magnetic potential Ψ and the electric potential Φ. Notice that inside the star, Φ traces the magnetic field lines $\Psi = {\rm cost}$ in agreement with the MHD requirement. Outside the star the structure of the electric potential is mainly quadrupolar reflecting the fact that the monopolar component has been filtered out in order to achieve a globally uncharged configuration. The resulting internal electric field strength reaches its maximum value between the rotational axis and the neutral lines, where it vanishes together with the magnetic field. The exterior electric field instead reaches its maximum strength in correspondence of the pole of the star. Obviously, different prescriptions on the total electric charge of the star lead to different morphologies for the exterior electric field. The interior one instead remains unchanged. Hence, the structure of the star is only marginally affected by the choice for the electrosphere. We postpone a discussion about the structure of the electrosphere to Section 4.2.4.

4.2.1 Results at fixed gravitational mass

Considering again a fixed gravitational mass $M = 1.551{\rm M}_\odot$, in Fig. 12 we show the variation of $\rho_{\rm c}$, M_0 and $R_{\rm c}$, with respect to

Downloaded from https://academic.oup.com/mnras/article-abstract/470/2/2469/3820933 by INAF Trieste (Osservatorio Astronomico di Trieste) user on 14 July 2020

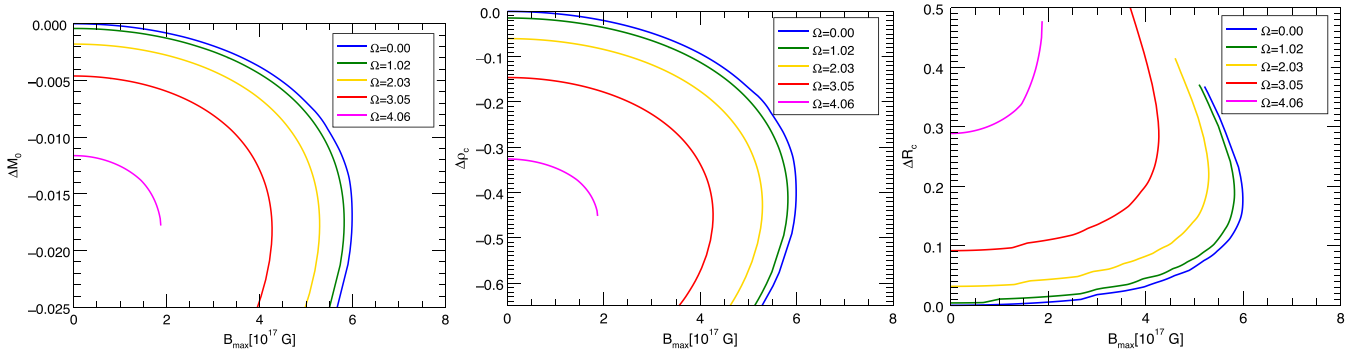

Figure 12. Variation of the baryon mass M_0, central density ρ_c and circumferential radius R_c with respect to the unmagnetized and static reference model, along sequences of constant gravitational mass $M = 1.55\mathrm{M}_\odot$ but different Ω, as a function of $B_{\max}$.

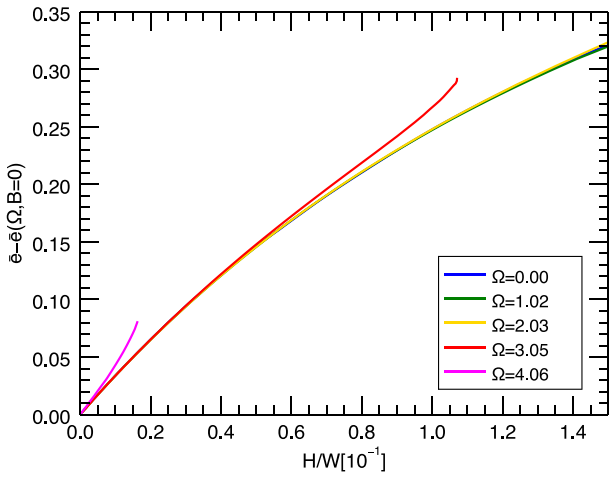

Figure 13. Variation of the deformation rate $\bar{e}$ with respect to the unmagnetized rotating reference configuration as a function of the magnetic to binding energy ratio along sequences with fixed mass $M = 1.55\mathrm{M}_\odot$.

the non-rotating and unmagnetized equilibrium configuration, as functions of $B_{\max}$ and Ω. Just as in the toroidal case, the qualitative effects of the poloidal magnetic field remain the same independently from the rotational rate: both the baryonic mass M_0 and the central density ρ_c decrease with $B_{\max}$ while the circumferential radius $R_{\rm circ}$ and the deformation rate $\bar{e}$ grow. As it was suggested in PBD14, the equilibrium sequences are characterized by a turning point in $B_{\max}$: the oblateness initially grows due to a rise of magnetic field, but, as soon as the maximum is reached, a further increase of the magnetization causes a rapid expansion of the equatorial radius and a rapid drop in the central density corresponding also to a reduction of the polar radius. In the end this leads to configurations with an off-centred density distribution. Interestingly, independently of Ω, the configuration at the turning point shows a circumferential radius $R_{\rm circ}$ about 20 per cent larger than the unmagnetized model and $\bar{e} \sim 0.3$.

As for the toroidal field case, the role of the rotation can be factored out as an offset, plus an enhancement of the effectiveness of the magnetic field and it is still possible to find self-similarity scaling. In particular equations (57) and (58) are still valid with $a_{\bar{e}} = -0.15$ and $b_{\bar{e}} = 0.27$, respectively, in the range $\Omega \lesssim 3 \times 10^3\ \mathrm{s}^{-1}$ and $T/M \lesssim 5 \times 10^{-3}$ as shown in Fig. 13. However while the sign of $a_{\bar{e}}$ remains the same as for purely toroidal configuration, the sign of $b_{\bar{e}}$ changes from negative to positive. This is because at a given H/W configurations with slower rotation have larger energy H resulting in a more evident deformation.

We remark that now the electromagnetic energy is not uniquely confined inside the star: ∼25 per cent of the total energy is located outside the star. Moreover, the contribution of the electric field to the global energy is at most of the order of few per cent, even for the fastest rotators.

In the range $B_{\max} \lesssim 3 \times 10^{17}$ G and $\Omega \lesssim 10^3\mathrm{s}^{-1}$ (corresponding to $H/W \lesssim 3.5 \times 10^{-2}$ and $T/W \lesssim 5.1 \times 10^{-2}$ or $H/M \lesssim 2.5 \times 10^{-3}$ and $T/M \lesssim 4.1 \times 10^{-3}$), which is comparable with the bilinear regime for the purely toroidal field case (see equations 59 and 60), the deformation rate $\bar{e}$ is approximated with an accuracy $\lesssim 10$ per cent by the relation

$$\bar{e} = d_\Omega\, \Omega^2_{\rm ms} + d_{\rm B}\, B^2_{17}, \tag{70}$$

where $d_{\rm B} \simeq 5.4 \times 10^{-3}$ and $d_\Omega \simeq 0.31$. Analogously, for the surface ellipticity we find

$$e_{\rm s} = s_\Omega\, \Omega_{\rm ms} + s_{\rm B}\, B^2_{17}, \tag{71}$$

with $s_{\rm B} \simeq 4.5 \times 10^{-3}$ and $s_\Omega \simeq 0.38$.

These scalings can be given also in term of the magnetic dipole moment μ that, in contrast with $B_{\max}$, it is a measurable quantity. In the same range as before we find

$$\bar{e} = d_\Omega\, \Omega^2_{\rm ms} + d_\mu\, \mu^2_{35}, \tag{72}$$

where $d_\mu = 0.14$ and

$$\bar{e} = s_\Omega\, \Omega^2_{\rm ms} + s_\mu\, \mu^2_{35}, \tag{73}$$

with $s_\mu \simeq 0.11$ (μ_{35} is the value of the magnetic dipole moment in unity of $10^{35}\ \mathrm{erG}^{-1}$). In Fig. 14, we show the variation of different stellar quantities as functions of μ. Notice that, just as the magnetic energy, μ is a monotonic function of the magnetization $k_{\rm pol}$. Moreover, in the case of ΔM_0, a parametrization in terms of μ reduces the non-linear coupling between rotation and magnetic field.

4.2.2 *The effects of the current distribution*

The addition of non-linear current terms to the system can substantially modify the structure of the magnetic field. In particular as discussed in BPD15 and PBD14 subtractive currents ($\xi < 0$ in equation 44) tend to concentrate the magnetic field towards the magnetic axis causing a simultaneous demagnetization of the outer layers. Additive current terms ($\xi > 0$), instead, act to concentrate the magnetic field towards the stellar surface, causing also a global

Downloaded from https://academic.oup.com/mnras/article-abstract/470/2/2469/3820933 by INAF Trieste (Osservatorio Astronomico di Trieste) user on 14 July 2020

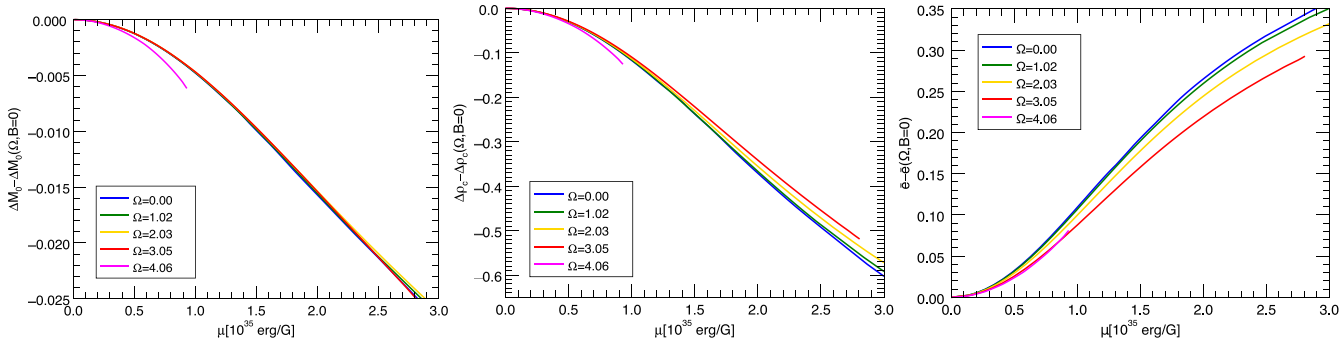

Figure 14. Variation of the baryonic mass M_0, central density ρ_c and deformation rate $\bar{e}$ as a function of the magnetic dipole moment μ along equilibrium configurations with fixed gravitational mass $M = 1.55\mathrm{M}_\odot$.

strengthening of the magnetic field. As a result, at a given value of $B_{\max}$, the presence of additive current gives a larger deformation $\bar{e}$; the opposite for subtractive ones.

An extensive investigation of the parameter space in the case of rotating models, using different prescription for the current distribution, is however computationally expensive. The non-linear current term substantially slows down the convergence of the scheme even in the static case, where we have just to solve the Grad–Shafranov equation. In order to get some handling on the effects of the current distribution on the deformation of the star, as we have done in the toroidal field case, we have just analysed the simple static case with $\nu = 1$, confident that in the bilinear regimes magnetic and rotation effects can be separated. Away from the fully saturated regime discussed in BPD15, in the range $|\xi| \lesssim 30$, we have found that the effects of the non-linear currents terms can be effectively reabsorbed with a parametrization in terms of H/W (or equivalently H/M) with an accuracy of ∼5 per cent, using an effective energy ratio

$$\bar{e} \simeq \mathcal{F}\left([1 + a_{\hat{\xi}}\xi]\frac{H}{W}\right), \tag{74}$$

where $a_{\hat{\xi}} = -2.8 \times 10^{-3}$. In the linear regime with $B_{\max} \lesssim 2. \times 10^{17}$G, the parametrization in term of the magnetic field strength can be generalized as

$$\bar{e} = [1 + d_{\hat{\xi}}\,\xi]\, d_{\rm B}\, B_{17}^2, \tag{75}$$

with $d_{\hat{\xi}} = 4.1 \times 10^{-3}$.

The difference between the signs of $a_{\hat{\xi}}$ and $d_{\hat{\xi}}$ may appear contradictory. This discrepancy is however only apparent since, for a fixed value of H/W, the configuration with $\xi < 0$ has a larger value of $B_{\max}$ than the configuration with $\xi > 0$. This is because subtractive currents demagnetize to outer layer of the star and, in order to achieve higher value of H/W, one has to increase the maximum strength of the magnetic field which in turn largely affects the core. This holds also in the fully saturated regime discussed in BPD15. Nevertheless, in this case, it is not possible to find a simple parametrization of the effects of the current distribution in terms of neither energy ratios nor other global quantities such as the magnetic dipole moment. Contrarily to toroidal configurations, here the morphology of the current distribution may play a role in affecting the structure of the NS. However, if parametrized in terms of H/W, the deformation of the fully saturated regime ranges just within a factor 2 (see also fig. B1 of BPD15).

4.2.3 *Trends at different gravitational mass*

As expected both the magnetic and rotational effects depend on the compactness of the star. To generalize the trends found in the previous sections we again make use of an effective energy ratio:

$$\left[\frac{H}{W}\right]_{\rm eff} = \frac{1.55\ \mathrm{M}_\odot}{M}\frac{H}{W}. \tag{76}$$

By using this quantity the induced deformation can be parametrized as in the equation (66), where the coupling term is now given by

$$a_{\bar{e},\rm eff} = -\left(2.5 - 2.4\frac{M}{1.55\ \mathrm{M}_\odot}\right), \tag{77}$$

while the functional form for $\mathcal{F}$ is provided by

$$\mathcal{F}(x) = 3.8x - 4.3x^{1.5}. \tag{78}$$

As shown in the left-hand panel of Fig. 15, this parametrization is able to describe the trends of the $\bar{e}$ up to ∼0.15 with an accuracy less than 5 per cent. Notice that here, as in the toroidal field case, for a fixed value of H/W the coupling term $a_{\bar{e},\rm eff}$ reduces the absolute value of $\bar{e}$.

Interestingly, a more accurate parametrization of $\bar{e}$ can be obtained including the circumferential radius in place of the gravitational mass. In particular we obtain that, by using the relation

$$\bar{e} \simeq 3.2\frac{T}{W}\bigg|_{B=0} + \mathcal{G}\left(\left[1 + c_{\bar{e},\rm eff}\Omega_{\rm ms}^2\right]\frac{H}{W}R_{14}\right), \tag{79}$$

where R_{14} is the circumferential radius normalized to 14km, the coupling term is given by

$$c_{\bar{e},\rm eff} = -3.6 + 3.0\frac{M}{1.55\ \mathrm{M}_\odot} \tag{80}$$

and the functional form of $\mathcal{G}$ is

$$\mathcal{G} = 4.8\,x - 5.1\,x^{1.3}, \tag{81}$$

we can fit with high accuracy the variation of $\bar{e}$ for all the value of $\Omega \lesssim 3 \times 10^3 \mathrm{s}^{-1}$ and M even in the strong magnetization regime as shown in Fig. 15.

Limited to the bilinear regime, the coefficients appearing in the equations (70)–(73) are listed in Table 5 as a function of the gravitational mass. Interestingly, the coefficients d_μ and s_μ are only weakly affected by the specific value of the gravitational mass and they remain almost constant within ∼5 per cent.

Downloaded from https://academic.oup.com/mnras/article-abstract/470/2/2469/3820933 by INAF Trieste (Osservatorio Astronomico di Trieste) user on 14 July 2020

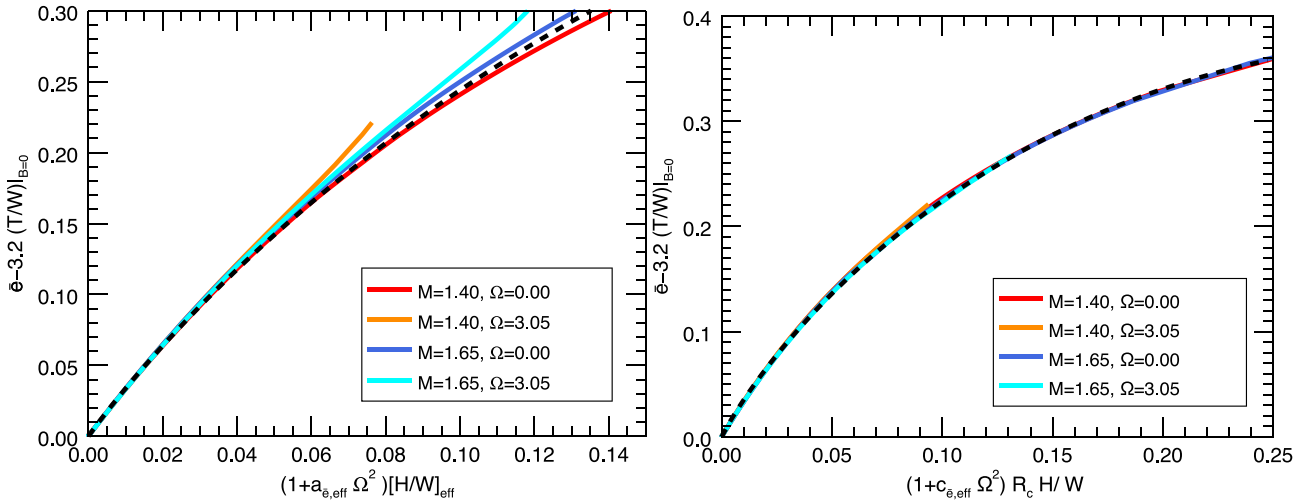

Figure 15. Deformation $\bar{e}$ with respect to the unmagnetized model as a function of the effective mass energy ratio H/W in the left-hand panel or HR_c/W (where R_c is normalized to 14 km) in the right-hand panel for configurations with mass between 1.40 and 1.65$M_\odot$ and rotational frequency $\Omega = 0.0$–$3.05 \times 10^3 s^{-1}$. The dashed black lines show equation (78) (left-hand panel) and equation (81) (right-hand panel).

Table 5. Mass dependence for the $\bar{e}$ expansion coefficients in the case of purely poloidal magnetic fields.

M $M_\odot$	d_Ω 10^{-1}	d_B 10^{-3}	d_μ 10^{-1}	s_Ω 10^{-1}	s_B 10^{-3}	s_μ 10^{-1}
1.40	4.5	9.8	1.4	6.0	9.0	1.1
1.45	4.0	8.1	1.4	5.1	7.9	1.1
1.50	3.6	6.7	1.4	4.6	5.9	1.1
1.55	3.1	5.4	1.4	3.8	4.5	1.1
1.60	2.8	4.4	1.4	3.5	3.9	1.1
1.65	2.3	3.2	1.4	3.1	3.0	1.1

In the perturbative regime of $H, T \to 0$ the relation in equation (66), with equation (77) and equation (78), gives:

$$\bar{e} = \frac{C_{\bar{e}}}{W_0}\left[T + 1.8\frac{H}{M/M_\odot}\right], \tag{82}$$

which is the analogous of equation (67) for the toroidal magnetic field. The main difference between the two relations is that in the poloidal field case the sign of the magnetic term is positive. This reflects the fact that a poloidal field induces an oblate deformation. An analogous relation is found also for the apparent ellipticity:

$$e_s = \frac{C_{e_s}}{W_0}\left[T + 1.1\frac{H}{M/M_\odot}\right]. \tag{83}$$

4.2.4 *The structure of the electrosphere*

The electric field outside the star is not fully determined by the ideal MHD condition equation (34), due to the arbitrary constant in the definition of the harmonic function Φ_a. Such degree of freedom corresponds to an arbitrary charge that can be added to the system in order to obtain different physical outer structures. As anticipated in Section 3.1, a typical choice is to consider a globally neutral NS (Goldreich & Julian 1969; Bocquet et al. 1995; Franzon & Schramm 2015; Franzon et al. 2016), but it is also possible to consider configurations where the charge distribution reduces the Lorentz force in the polar region (Michel 1974) or minimizes the energy content of the electrosphere (Ruffini & Treves 1973).

For simplicity in the following we limit our analysis to the weak magnetization and slow rotation limit, since in this regime the electromagnetic field does not alter substantially the structure of the NS, and the solution can be rescaled with B_{max} up to 10^{16} G. General trends, however, remain valid even at larger magnetic fields.

In the left-hand panel of Fig. 16, we show the electric field strength for a globally uncharged NS. In this case the external electric field peaks at the pole, in the polar cap, i.e. the region of magnetic field lines extending to infinity beyond the Light Cylinder. In principle, these electric fields are able to extract particle from the surface into the magnetosphere and beyond, charging the NS itself. In the right-hand panel of the same figure, we show a configuration for a NS where the electric field vanishes at the poles. The NS is endowed with a net electric charge corresponding to $Q_e \simeq 10^{24} B_{pole,\,14}\,\Omega_{100}$ statC (here $B_{pole,\,14}$ and Ω_{100} are the magnetic field at the pole in units of 10^{14} G and the rotation rate in units of $100\,s^{-1}$, respectively). Notice that Q_e is still far below the critical value $\sim 10^{29}$ statC (i.e. $\sim 0.1\sqrt{G}M_0$ in cgs units) capable to induce substantial effects in the stellar structure (Ghezzi 2005). The electric field now peaks at the stellar equator, where it is a factor $\sim$2 stronger than the internal one. Although this star is unable to extract particles from polar caps, it can in principle attract them from regions beyond the magnetosphere. Interestingly comparing configurations with different Q_e we have find that the configuration that minimizes the electromagnetic energy in the electrosphere is the uncharged one. This is in contrast with the results obtained in Ruffini & Treves (1973), where the minimum energy configuration has a negative net charge. In that work however, the structure of the magnetic field was chosen to depend on the specific value of the electric charge.

In all cases the normal component of the electric field at the surface shows a discontinuity corresponding to a surface charge density

$$\sigma_e = E^r_{out} - E^r_{in}, \tag{84}$$

where E^r_{out} and E^r_{in} are the radial components of the surface electric field inside and outside the NS, respectively. The profile of σ_e for the configurations presented in Fig. 16 is shown in Fig. 17 (numerical values are normalized to the Goldreich–Julian density $\sigma_{GJ} = \Omega B_{pole} r_p = 9.5 \times 10^{10}$statCcm^{-2}). Notice that the sign

Downloaded from https://academic.oup.com/mnras/article-abstract/470/2/2469/3820933 by INAF Trieste (Osservatorio Astronomico di Trieste) user on 14 July 2020

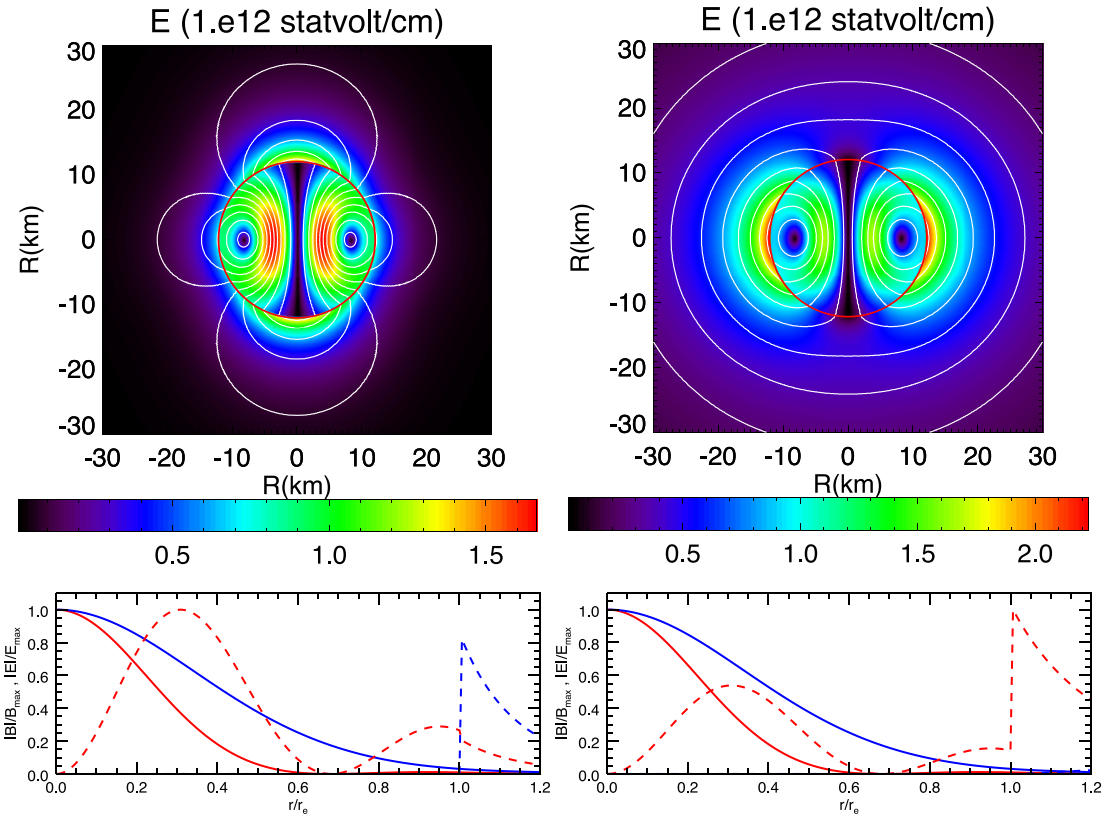

Figure 16. Top panels: distribution of the electric field strength $E = \sqrt{E^r E_r + E^\theta E_\theta}$ together with the isocontours of the potential Φ for configurations with vanishing net electric charge (left-hand panels) and vanishing polar electric field (right-hand panels) for a NS having $M = 1.55 M_\odot$, $\Omega = 200\,\mathrm{s}^{-1}$, $B_{\max} = 8.4 \times 10^{14}$ G and $B_{\rm pole} = 1.5 \times 10^{14}$ G. Bottom panels: radial profiles of the magnetic (solid lines) and electric (dashed lines) field strength along the equatorial (red lines) and the polar direction (blue lines).

of the surface charge, as well as the sign of the electric field, depends on the relative orientation of the magnetic dipole moment and the angular momentum (our results are shown in the aligned case). As a consequence the sign of the associated Lorentz force acting on the surface, $L^i = \sigma_e E^i$, does not change. The latter is also shown in Fig. 17, where we plot both the orthogonal and the parallel component with respect to the magnetic field and where it is possible to see that, inside the star, the MHD condition guarantees that the parallel component of the Lorentz force vanishes.

In the uncharged configurations the charge surface density is maximal at the pole. The Lorentz force with respect to $E_{\rm in}$ vanishes on the rotation axis, reaches its maximum strength at latitude $\sim \pm 50$ deg and points always towards the equator, remaining mainly tangential to the stellar surface. The Lorentz force with respect to the external electric field instead is mainly parallel to the magnetic field in the polar region, and becomes mainly orthogonal in the equatorial region where it points inward. In the case of a negative surface charge (an electron excess if angular momentum and dipole moment are aligned), the Lorentz force is able to extract electrons. In the case of a positive surface charge (an ion excess if angular momentum and dipole moment are counter-aligned), the Lorentz force will be unable to extract ions. Indeed, assuming a cohesive energy $\sim$350keV for an iron chain with spacing $\sim 10^{-9}$cm at $B = 10^{14}$G (Medin & Lai 2006, 2007), the critical electric field capable to directly rip iron ions off the stellar crust is of the order of $\sim 10^{13-14}$statV cm^{-1} which is larger than the electric fields of our model ($\sim 10^{12-13}$statV cm^{-1} up to millisecond rotation).

The configuration with a vanishing polar Lorentz force is instead characterized by a surface charge density of opposite sign, with respect to the uncharged case, with a maximum at the equator. By consequence, the action of the surface Lorentz force is reversed: the maximum strength is reached in the equatorial region, and the force always points towards the exterior. Hence, if the surface charge is made of electrons (counter-aligned case), such force could pull them out from the surface and fill the closed magnetosphere within the Light Cylinder.

For a star described in terms of an ideal fluid, it is not possible to balance the surface Lorenz force, because no stress is present to counteract its tangential component. In the presence of an elastic crust, on the other hand, a crustal deformation can give rise to stresses strong enough to balance the Lorentz force. In principle, the overall Lorentz force may act to stretch the crust of the NS favouring a prolate deformation, in the uncharged case, or an oblate deformation in the case of no polar Lorentz force. To estimate the crustal displacement required to balance the Lorenz force, we have solved the equations for the isostatic-like equilibrium of an elastic spherical thin shell (see Tanimoto 1997 or Tanimoto 1998) subject to a surface force, and taking into account also the role of buoyancy. We assume a typical crust thickness of $\sim$1km, a density at the base of the crust $\sim 10^{11}$ g cm^{-3} and Young modulus $\simeq 3 \times 10^{27}$ erg cm^{-3} (Chamel & Haensel 2008). We find that the vertical displacement is completely determined by buoyancy, and crustal elasticity plays a negligible effect. The amplitude of the vertical displacement is $|\Delta u_r| \simeq 6 \times 10^{-4} (B_{\rm pole,\,14}\Omega_{100})^2$ cm while for the tangential one is $|\Delta u_\theta| \simeq 6 \times 10^{-2} (B_{\rm pole,\,14}\Omega_{100})^2$ cm. Such vertical displacement is

Downloaded from https://academic.oup.com/mnras/article-abstract/470/2/2469/3820933 by INAF Trieste (Osservatorio Astronomico di Trieste) user on 14 July 2020

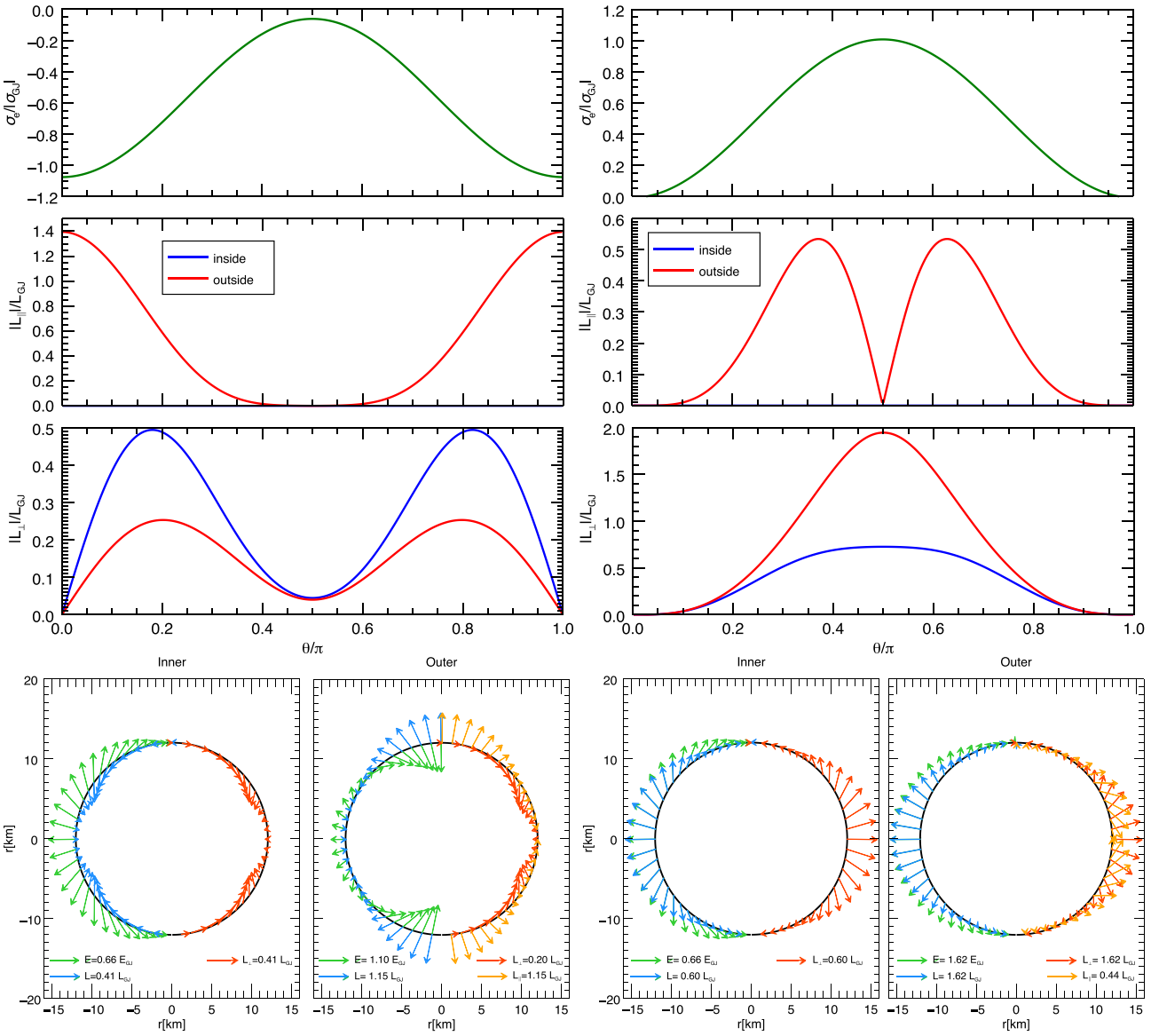

Figure 17. Top rows: trends of the surface charge density, of the parallel $|L_{\parallel}|$ and perpendicular component $|L_{\perp}|$ of the Lorentz force along the surface of the star as a function of the colatitude (parallel and perpendicular refer to the direction of the magnetic field) for the same configurations shown in Fig. 16. Bottom row: vector plots of the surface electric field $E^{\hat{i}}$, of the Lorentz force $L^{\hat{i}}$ and its perpendicular and parallel component. Numerical values are normalized to $\sigma_{\rm GJ} = E_{\rm GJ} = \Omega B_{\rm pole} r_{\rm p}$ and $L_{\rm GJ} = \rho_{\rm GJ} E_{\rm GJ}$ (corresponding respectively to $\sigma_{\rm GJ} = 9.5 \times 10^{10}$statCcm^{-2}, $E_{\rm GJ} = 1.2 \times 10^{12}$statVoltcm^{-1} and $L_{\rm GJ} = 1.1 \times 10^{23}$ dyne cm^{-2}). Panels on the left refers to the uncharged equilibrium configuration while panels on the right refers to the configuration with vanishing polar electric field.

negligible with respect to the one due to the global surface ellipticity derivable from equation (71), $|\Delta u| \simeq (1.2\,\Omega_{100}^2 + 0.46\,B_{\rm max,14}^2)$ cm. There is also a crustal quadrupole moment associated with such vertical displacement $|\bar{e}| \simeq 4 \times 10^{-13} (B_{\rm pole,14}\,\Omega_{100})^2$, which again can be shown to be negligible with respect to the global one as derivable from equation (70).

Let us finally point here that once one allows for the presence of a singular surface charge (and the related Lorentz force) in the Maxwell equations equation (22), then there is no reason to exclude the presence of any singular surface current. This is however usually done in building equilibrium models, because it guarantees the integrability for non-rotating system and avoids the problem to consider arbitrary crustal currents that in general are not well constrained by physical arguments. On the other hand, the extra degree of freedom associated with a surface current can be used to modify the magnetic field structure, and the net Lorentz force at the surface. In particular if one chooses the following surface current:

$$J_{\rm surf} = \sigma_e \frac{\Omega - \omega}{\alpha} \delta(r - r_{\rm e}), \tag{85}$$

corresponding to the assumption that the surface charge corotates with the star, then a discontinuity in the azimuthal component of the magnetic field arises:

$$J_{\rm surf} = \frac{B^{\theta}_{\rm in} - B^{\theta}_{\rm out}}{\psi^2 \sin\theta}. \tag{86}$$

As we have numerically verified through the computation of a model including $J_{\rm surf}$, both the radial and azimuthal component of the

Downloaded from https://academic.oup.com/mnras/article-abstract/470/2/2469/3820933 by INAF Trieste (Osservatorio Astronomico di Trieste) user on 14 July 2020

Table 6. Summary of the global relations for the deformation ratio $\bar{e}$ in terms of the rotational energy ratio T/W and the magnetic energy ratio H/W. $M_{1.5}$ and R_{14} are respectively the gravitational mass and the circumferential radius in unity of $1.55\,\mathrm{M}_\odot$ and 14 km.

Purely toroidal	$\bar{e} \simeq 3.2\frac{T}{W}\Big\vert_{B=0} - 2.7x - 0.068(10x)^{3.2}$	with	$x = \left(0.84 + \frac{0.16}{m}\right)\left[1 - (3.94 - 2.98M_{1.5})\,\Omega^2_{\rm ms}\right] M_{1.5}^{-1}\frac{H}{W}$
Purely poloidal	$\bar{e} \simeq 3.2\frac{T}{W}\Big\vert_{B=0} + 3.8x - 4.3x^{1.5}$	with	$x = \left[1 - (2.5 - 2.4M_{1.5})\,\Omega^2_{\rm ms}\right] M_{1.5}^{-1}\frac{H}{W}$
	$\bar{e} \simeq 3.2\frac{T}{W}\Big\vert_{B=0} + 4.8x - 5.1x^{1.3}$	with	$x = \left[1 - (3.6 - 3.0M_{1.5})\,\Omega^2_{\rm ms}\right] R_{14}\frac{H}{W}$

surface Lorentz force with respect to the internal electromagnetic field now vanish. The surface charge and current are now in equilibrium with respect to the internal field. Notice however that, outside the star, no current can suppress the component of the Lorentz force parallel to the magnetic field. Finally, this current term induces only small deviation $\lesssim 10^{-5}$ on the global structure of the electromagnetic field. The relevant effect is on the Lorentz force itself.

5 DISCUSSION AND CONCLUSION

In this work, we present models of rotating magnetized NSs extending our previous results obtained in the static case (PBD14, BPD15; Pili et al. 2015). Our extensive investigation of the parameter space has allowed us to establish new quantitative and qualitative relations among different quantities of interest (such as the gravitational and baryonic mass, the energy content of the system, the current distribution) giving particular emphasis to the characterization and the parametrization of the stellar deformation $\bar{e}$. This is indeed the relevant quantities in the context of GWs astronomy, especially for newly born magnetars. Previous works (e.g. Bocquet et al. 1995; Haskell et al. 2008; FR12) have already provided similar parametrizations, both in terms of the magnetic field strength and the rotational rate or in terms of the associated energetics. However, in the majority of cases, they were limited to either the Newtonian or the perturbative regime, or to a limited set of reference masses. Here, we have generalized such results up to the fully non-linear regime for a wide range of masses (excluding supramassive configurations) and current distributions.

In the bilinear regime the coupling between magnetic and centrifugal effects can be safely neglected and the stellar deformation can be accurately evaluated in terms of the magnetic field strength and the rotational rate through equations (62) and (70) or, equivalently, in terms of the energetic content of the system using equations (67) and (82). The deformability of the star mostly depends on the compactness of the star itself. As shown also in Tables 3 and 5, the deformation coefficients decrease with the mass or the gravitational binding energy of the star. This is indicative of the fact that the magnetic field is more efficient in less compact configurations with smaller central densities and larger radii. Similar trends were also observed in FR12 where, varying the EoS at fixed gravitational mass, the deformation coefficients grow with the stellar radius (notice that our results coincide with those of FR12 in the case of $M = 1.4\,\mathrm{M}_\odot$). Interestingly, for purely poloidal field, we have find that the deformation coefficient relative to the magnetic dipole moment d_μ weakly depends on the specific value of the mass, and it can be considered constant within ∼5 per cent. As a consequence the ratio between the magnetic and the gravitational spin-down time-scales (respectively $\tau_{\rm d} \propto \mu^2$ and $\tau_{\rm GW} \propto \bar{e} \sim d_\mu^2\mu^2$) can be expressed as a function of the magnetic dipole moment and the rotational rate. In particular in the case of orthogonal rotation one obtains $\tau_{\rm d}/\tau_{\rm GW} \sim 6 \times 10^{-2}\mu_{35}^2\Omega_{\rm ms}$.

Comparing the purely toroidal/poloidal case, and in particular equations (67) and (82), it is apparent that, being the magnetic energy the same, a poloidal magnetic field is more effective in deforming the star than the toroidal one. The situation is reversed if we look at the deformation in terms of the magnetic field strength, i.e. if we compare the absolute values of $d_{\rm B}$. This is due to the fact that, at a given value for the magnetic field strength, the toroidal configuration has typically a larger energy.

We can now establish the conditions favouring an efficient production of GWs. By considering the direct sum of the deformations induced by the two component separately, we can roughly evaluate the total deformation induced by a mixed field. According to Dall'Osso et al. (2009), we found that in the case of a newly born millisecond magnetar with a dipolar field of the order of 10^{14} G and an internal toroidal field of $\sim 10^{16}$G, if the spin-flip mechanism occurs, the star gives rise to an observable GWs emission.

Away from the bilinear regime the magnetic induced deformation cannot be determined without considering also the coupling effects with the rotation. This, reducing the compactness of the star, actually enhances the effectiveness of the magnetic field. Moreover, the joint effects of a toroidal magnetic field and the rotation can substantially reduce the frequency of mass-shedding, or determine characteristic solutions with oblate surface deformation but globally prolate deformation (the transition $\bar{e} < 0$ occurs near equipartition $H/T \sim 0.8M/\mathrm{M}_\odot$ while the transition to $e_{\rm s} < 0$ is at $H/T \sim 4M/\mathrm{M}_\odot$). In the case of purely toroidal field, the surface Lorentz force acts to stabilize the system against mass-shedding (in line with the results by Franzon & Schramm 2015). In principle, in this case, one should also consider deformations due to the surface Lorentz stresses that, depending on the net charge of the NS, may counterbalance or enhance the global deformation. However, our simple estimation suggests that crustal deformation are generally negligible unless one considers millisecond rotators and high magnetization with $B_{\rm pole} > 10^{17}$ G. Hence our general results, and in particular the extrapolation to the bilinear regime, are not affected by the unbalanced surface stresses.

Interestingly we find that, in spite of the great complexity of the space of the solutions, a parametrization of the induced deformation in terms of H/W and T/W allows us to reabsorb the dependence on the current distribution, the rotation and the compactness of the star in unique scaling laws(summarized in Table 6 for the reader's convenience), that hold up to the fully non-linear regime with an accuracy $\lesssim 5$ per cent. This kind of self-similarity suggests that apart from small residual effects, the stellar deformation is more sensible to the ratio of the magnetic and rotational energy to the gravitational binding energy rather than the current distribution. Unfortunately, this behaviour fails if one considers fully saturated or strongly

Downloaded from https://academic.oup.com/mnras/article-abstract/470/2/2469/3820933 by INAF Trieste (Osservatorio Astronomico di Trieste) user on 14 July 2020

concentrated currents as those presented in BPD15. Being the energetics the same, concentrated currents located deeper inside the star are indeed more effective than currents located in the outer layers. This has also important consequences in the case of mixed field configuration. Reanalysing the TT equilibrium sequences presented in PBD14, we have verified that the deformation induced by a mixed field cannot be trivially described as a direct sum of deformations induced by the toroidal and poloidal component separately. As discussed in BPD15, in our TT models the interplay between the two fields causes a rearrangement of the currents that tend to concentrate towards the surface. As a result even a weakly energetic toroidal field (with $H_{\rm tor} \lesssim 10$ per cent$H_{\rm tot}$) is able to induce, at a given total energy $H_{\rm tot}$, a substantial reduction (of the order of 40 per cent for our models) of the oblateness of the star. This is in agreement with Mastrano et al. (2015). Computing TT models for non-barotropic NSs, they showed how it is possible to reduce the effectiveness of the poloidal/toroidal component, augmenting the weight of the quadrupolar component of the poloidal magnetic field or enlarging the volume occupied by the toroidal field. Hence, in general, the condition $\bar{e} = 0$ is not reached at equipartition $H_{\rm pol} = H_{\rm tor}$ but it strongly depends on the current distribution. This may also suggests that the work done by the Lorentz force, evaluated as a volume integral of the Lorentz force itself (e.g. as in Fujisawa & Eriguchi 2013 or Fujisawa et al. 2013, including also the contribution of possible unbalanced magnetic surface stresses), could be a more natural parameter to choose rather than the magnetic energy. Indeed it directly encodes a dependence on the currents distribution, distinguishing between the force-free and non-force-free component of the magnetic field (Fujisawa & Eriguchi 2015).

It is finally clear that, in order to provide a more realistic estimation of the expected GWs emission from newly born millisecond magnetars, one needs to know in detail the current distribution arising from the amplification of the magnetic field during core collapse. However if that currents are distributed rather than localized, we might expect that the direct addition of the deformations produced independently by the two component of the field gives a reasonable estimation of the global deformation.

ACKNOWLEDGEMENTS

The authors acknowledge support from the INFN-TEONGRAV initiative and from the INFN-CIPE grant *High performance data network: convergenza di metodologie e integrazione di infrastrutture per HPC e HTC*. LDZ also acknowledges support from the PRIN-MIUR project prot. 2015L5EE2Y *Multiscale simulations of high-energy astrophysical plasmas*. This work has also been supported by an EU FP7-CIG grant issued to the NSMAG project (PI: NB).

REFERENCES

Akgün T., Reisenegger A., Mastrano A., Marchant P., 2013, MNRAS, 433, 2445
Alcubierre M., 2008, Introduction to 3+1 Numerical Relativity. Oxford Univ. Press, Oxford
Armaza C., Reisenegger A., Alejandro Valdivia J., 2015, ApJ, 802, 121
Arnowitt R. L., Deser S., Misner C. W., 1962, Recent Developments in General Relativity. Polish Scientific Publishers, Warsaw, p. 127
Baumgarte T. W., Shapiro S. L., 2010, Numerical Relativity: Solving Einstein's Equations on the Computer. Cambridge Univ. Press, Cambridge
Bera P., Bhattacharya D., 2014, MNRAS, 445, 3951
Bera P., Bhattacharya D., 2016, MNRAS, 456, 3375
Bocquet M., Bonazzola S., Gourgoulhon E., Novak J., 1995, A&A, 301, 757
Bonanno A., Rezzolla L., Urpin V., 2003, A&A, 410, L33
Bonazzola S., Gourgoulhon E., 1996, A&A, 312, 675
Braithwaite J., 2009, MNRAS, 397, 763
Braithwaite J., Spruit H. C., 2006, A&A, 450, 1097
Bucciantini N., Del Zanna L., 2011, A&A, 528, A101
Bucciantini N., Del Zanna L., 2013, MNRAS, 428, 71
Bucciantini N., Quataert E., Metzger B. D., Thompson T. A., Arons J., Del Zanna L., 2009, MNRAS, 396, 2038
Bucciantini N., Metzger B. D., Thompson T. A., Quataert E., 2012, MNRAS, 419, 1537
Bucciantini N., Pili A. G., Del Zanna L., 2015, MNRAS, 447, 3278 (BPD15)
Burrows A., Lattimer J. M., 1986, ApJ, 307, 178
Burrows A., Dessart L., Livne E., Ott C. D., Murphy J., 2007, ApJ, 664, 416
Camelio G., Gualtieri L., Pons J. A., Ferrari V., 2016, Phys. Rev. D, 94, 024008
Cardall C. Y., Prakash M., Lattimer J. M., 2001, ApJ, 554, 322
Carter B., 1969, J. Math. Phys., 10, 70
Carter B., 1970, Commun. Math. Phys., 17, 233
Carter B., 1973, in Dewitt C., Dewitt B. S., eds, Black Holes (Les Astres Occlus). Gordon and Breach, New York, p. 57
Chamel N., Haensel P., 2008, Living Rev. Relativ., 11, 10
Chatterjee D., Elghozi T., Novak J., Oertel M., 2015, MNRAS, 447, 3785
Ciolfi R., Rezzolla L., 2013, MNRAS, 435, L43
Ciolfi R., Ferrari V., Gualtieri L., Pons J. A., 2009, MNRAS, 397, 913
Ciolfi R., Ferrari V., Gualtieri L., 2010, MNRAS, 406, 2540
Clark J. S., Ritchie B. W., Najarro F., Langer N., Negueruela I., 2014, A&A, 565, A90
Contopoulos I., Kazanas D., Fendt C., 1999, ApJ, 511, 351
Cordero-Carrión I., Cerdá-Durán P., Dimmelmeier H., Jaramillo J. L., Novak J., Gourgoulhon E., 2009, Phys. Rev. D, 79, 024017
Cutler C., 2002, Phys. Rev. D, 66, 084025
Dall'Osso S., Shore S. N., Stella L., 2009, MNRAS, 398, 1869
Das U., Mukhopadhyay B., 2015, J. Cosmol. Astropart. Phys., 5, 16
Del Zanna L., Zanotti O., Bucciantini N., Londrillo P., 2007, A&A, 473, 11
Del Zanna L., Papini E., Landi S., Bugli M., Bucciantini N., 2016, MNRAS, 460, 3753
Dimmelmeier H., Font J. A., Müller E., 2002, in Gurzadyan V. G., Jantzen R. T., Ruffini R., eds, The Ninth Marcel Grossmann Meeting, Recent Developments in Theoretical and Experimental General Relativity, Gravitation and Relativistic Field Theories. World Scientific Press, Singapore, p. 1695
Dimmelmeier H., Stergioulas N., Font J. A., 2006, MNRAS, 368, 1609
Drago A., Pagliara G., 2015, Phys. Rev. C, 92, 045801
Duncan R. C., Thompson C., 1992, ApJ, 392, L9
Ferrario L., Wickramasinghe D., 2006, MNRAS, 367, 1323
Ferrario L., Wickramasinghe D., 2008, MNRAS, 389, L66
Ferrario L., Melatos A., Zrake J., 2015, Space Sci. Rev., 191, 77
Franzon B., Schramm S., 2015, Phys. Rev. D, 92, 083006
Franzon B., Dexheimer V., Schramm S., 2016, Phys. Rev. D, 94, 044018
Frieben J., Rezzolla L., 2012, MNRAS, 427, 3406 (FR12)
Fujisawa K., 2015, MNRAS, 450, 4016
Fujisawa K., Eriguchi Y., 2013, MNRAS, 432, 1245
Fujisawa K., Eriguchi Y., 2015, PASJ, 67, 53
Fujisawa K., Kisaka S., 2014, MNRAS, 445, 2777
Fujisawa K., Yoshida S., Eriguchi Y., 2012, MNRAS, 422, 434
Fujisawa K., Takahashi R., Yoshida S., Eriguchi Y., 2013, MNRAS, 431, 1453
Ghezzi C. R., 2005, Phys. Rev. D, 72, 104017
Giacomazzo B., Zrake J., Duffell P. C., MacFadyen A. I., Perna R., 2015, ApJ, 809, 39
Gilkis A., 2016, preprint (arXiv:1608.05320)
Glampedakis K., Lander S. K., Andersson N., 2014, MNRAS, 437, 2
Goldreich P., Julian W. H., 1969, ApJ, 157, 869
Gourgoulhon E., 2007, 3 + 1 formalism in general relativity: bases of numerical relativity. Vol. 846. Springer Science & Business Media
Gourgoulhon E., 2010, preprint (arXiv:1003.5015)

Downloaded from https://academic.oup.com/mnras/article-abstract/470/2/2469/3820933 by INAF Trieste (Osservatorio Astronomico di Trieste) user on 14 July 2020

Goussard J.-O., Haensel P., Zdunik J. L., 1998, A&A, 330, 1005
Haskell B., Samuelsson L., Glampedakis K., Andersson N., 2008, MNRAS, 385, 531
Heger A., Woosley S. E., Spruit H. C., 2005, ApJ, 626, 350
Ioka K., Sasaki M., 2004, ApJ, 600, 296
Isenberg J. A., 2008, Int. J. Mod. Phys. D, 17, 265
Kiuchi K., Yoshida S., 2008, Phys. Rev. D, 78, 044045
Kiuchi K., Cerdá-Durán P., Kyutoku K., Sekiguchi Y., Shibata M., 2015, Phys. Rev. D, 92, 124034
Konno K., 2001, A&A, 372, 594
Kundt W., Trümper M., 1966, Z. Phys., 192, 419
Lander S. K., Jones D. I., 2009, MNRAS, 395, 2162
Lasky P. D., Glampedakis K., 2016, MNRAS, 458, 1660
Lasky P. D., Melatos A., 2013, Phys. Rev. D, 88, 103005
Mastrano A., Melatos A., Reisenegger A., Akgün T., 2011, MNRAS, 417, 2288
Mastrano A., Suvorov A. G., Melatos A., 2015, MNRAS, 447, 3475
Medin Z., Lai D., 2006, Phys. Rev. A, 74, 062507
Medin Z., Lai D., 2007, MNRAS, 382, 1833
Metzger B. D., Giannios D., Thompson T. A., Bucciantini N., Quataert E., 2011, MNRAS, 413, 2031
Michel F. C., 1973, ApJ, 180, L133
Michel F. C., 1974, Phys. Rev. Lett., 33, 1521
Michel F. C., Li H., 1999, Phys. Rep., 318, 227
Mitchell J. P., Braithwaite J., Reisenegger A., Spruit H., Valdivia J. A., Langer N., 2015, MNRAS, 447, 1213
Moriya T. J., Tauris T. M., 2016, MNRAS, 460, L55
Mösta P., Ott C. D., Radice D., Roberts L. F., Schnetter E., Haas R., 2015, Nature, 528, 376
Mukhopadhyay B., 2016, preprint (arXiv:1609.01862)
Muno M. P. et al., 2006, ApJ, 636, L41
Nakamura K., Kuroda T., Takiwaki T., Kotake K., 2014, ApJ, 793, 45
Oron A., 2002, Phys. Rev. D, 66, 023006
Ott C. D., Burrows A., Thompson T. A., Livne E., Walder R., 2006, ApJS, 164, 130
Ott C. D., Dimmelmeier H., Marek A., Janka H.-T., Zink B., Hawke I., Schnetter E., 2007, Class. Quantum Gravity, 24, S139
Pétri J., 2016, MNRAS, 456, 4455
Pili A. G., Bucciantini N., Del Zanna L., 2014, MNRAS, 439, 3541 (PBD14)
Pili A. G., Bucciantini N., Del Zanna L., 2015, MNRAS, 447, 2821
Pili A. G., Bucciantini N., Drago A., Pagliara G., Del Zanna L., 2016, MNRAS, 462, L26
Pons J. A., Reddy S., Prakash M., Lattimer J. M., Miralles J. A., 1999, ApJ, 513, 780
Popov S. B., 2016, Astron. Astrophys. Trans., 29, 183
Popov S. B., Prokhorov M. E., 2006, MNRAS, 367, 732
Rea N., Gullón M., Pons J. A., Perna R., Dainotti M. G., Miralles J. A., Torres D. F., 2015, ApJ, 813, 92
Rheinhardt M., Geppert U., 2005, A&A, 435, 201
Rowlinson A., Gompertz B. P., Dainotti M., O'Brien P. T., Wijers R. A. M. J., van der Horst A. J., 2014, MNRAS, 443, 1779
Ruderman M., 1972, ARA&A, 10, 427
Ruffini R., Treves A., 1973, Astrophys. Lett., 13, 109
Ruiz M., Paschalidis V., Shapiro S. L., 2014, Phys. Rev. D, 89, 084045
Shibata M., Sekiguchi Y.-I., 2005, Phys. Rev. D, 72, 044014
Spitkovsky A., 2006, ApJ, 648, L51
Spruit H. C., 2008, in Bassa C., Wang Z., Cumming A., Kaspi V. M., eds, AIP Conf. Ser. Vol. 983, 40 Years of Pulsars: Millisecond Pulsars, Magnetars and More. Am. Inst. Phys., New York, p. 391
Spruit H. C., 2009, in Strassmeier K. G., Kosovichev A. G., Beckman J. E., eds, cIAU Symp. Vol. 259, Cosmic Magnetic Fields: From Planets, to Stars and Galaxies, Cambridge univ. press, Cambridge, p. 61
Staff J. E., Ouyed R., Jaikumar P., 2006, ApJ, 645, L145
Subramanian S., Mukhopadhyay B., 2015, MNRAS, 454, 752
Takiwaki T., Kotake K., Suwa Y., 2016, MNRAS, 461, L112
Tanimoto T., 1997, Geophys. J. Int., 129, 305
Tanimoto T., 1998, Geophys. J. Int., 134, 199
Tchekhovskoy A., Spitkovsky A., Li J. G., 2013, MNRAS, 435, L1
Timokhin A. N., 2006, MNRAS, 368, 1055
Tolman R. C., 1939, Phys. Rev., 55, 364
Urpin V., 2010, A&A, 509, A35
Urybaru K., Gourgoulhon E., Markakis C. M., Fujisawa K., Tsokaros A., Eriguchi Y., 2014, Phys. Rev. D, 90, 101501
Usov V. V., 1992, Nature, 357, 472
Viganò D., Rea N., Pons J. A., Perna R., Aguilera D. N., Miralles J. A., 2013, MNRAS, 434, 123
Villain L., Pons J. A., Cerdá-Durán P., Gourgoulhon E., 2004, A&A, 418, 283
von Zeipel H., 1924, MNRAS, 84, 665
Wilson J. R., Mathews G. J., 2003, Relativistic Numerical Hydrodynamics. Cambridge Univ. Press, Cambridge, p. 232
Woltjer L., 1960, ApJ, 131, 227
Yoon S.-C., 2015, PASA, 32, e015
Yoshida S., Eriguchi Y., 2006, ApJS, 164, 156

This paper has been typeset from a TEX/LATEX file prepared by the author.

Downloaded from https://academic.oup.com/mnras/article-abstract/470/2/2469/3820933 by INAF Trieste (Osservatorio Astronomico di Trieste) user on 14 July 2020